

EVIDENCE FOR AN INTERACTION BETWEEN THE GALACTIC CENTER CLOUDS: M0.10–0.08 AND M0.11–0.11

NATALIE O. BUTTERFIELD,^{1,2} CORNELIA C. LANG,³ ADAM GINSBURG,⁴ MARK R. MORRIS,⁵ JÜRGEN OTT,⁶ AND DOMINIC A. LUDOVICI⁷

¹*Department of Physics, Villanova University, 800 E. Lancaster Ave., Villanova, PA 19085, USA*

²*National Radio Astronomy Observatory, 520 Edgemont Road, Charlottesville, VA 22903, USA*

³*Department of Physics and Astronomy, University of Iowa, 30 North Dubuque Street, Iowa City, IA 52242, USA*

⁴*Department of Astronomy, University of Florida, PO Box 112055, USA*

⁵*Department of Physics & Astronomy, University of California, 430 Portola Plaza, Los Angeles, CA 90095, USA*

⁶*National Radio Astronomy Observatory, 1003 Lopezville Road, Socorro, NM 87801, USA*

⁷*Department of Physics and Engineering Science, Coastal Carolina University, 100 Chanticleer Dr E, Conway, SC 29528, USA*

ABSTRACT

We present high-resolution ($\sim 2\text{--}3''$; ~ 0.1 pc) radio observations of the Galactic center cloud M0.10–0.08 using the Very Large Array at K and Ka band (~ 25 and 36 GHz). The M0.10–0.08 cloud is located in a complex environment near the Galactic center Radio Arc and the adjacent M0.11–0.11 molecular cloud. From our data, M0.10–0.08 appears to be a compact molecular cloud (~ 3 pc) that contains multiple compact molecular cores ($5+$; < 0.4 pc). In this study we detect a total of 15 molecular transitions in M0.10–0.08 from the following molecules: NH_3 , HC_3N , CH_3OH , HC_5N , CH_3CN , and OCS . We have identified more than sixty 36 GHz CH_3OH masers in M0.10–0.08 with brightness temperatures above 400 K and 31 maser candidates with temperatures between $100\text{--}400$ K. We conduct a kinematic analysis of the gas using NH_3 and detect multiple velocity components towards this region of the Galactic center. The bulk of the gas in this region has a velocity of 51.5 km s^{-1} (M0.10–0.08) with a lower velocity wing at 37.6 km s^{-1} . We also detect a relatively faint velocity component at 10.6 km s^{-1} that we attribute to being an extension of the M0.11–0.11 cloud. Analysis of the gas kinematics, combined with past X-ray fluorescence observations, suggests M0.10–0.08 and M0.11–0.11 are located in the same vicinity of the Galactic center and could be physically interacting.

Keywords: Galaxy: center, ISM: kinematics and dynamics

1. INTRODUCTION

The central 200 pc of the galaxy (Central Molecular Zone; CMZ) is an extreme Galactic environment. Molecular clouds in the CMZ have hotter average gas temperatures ($50\text{--}300$ K; Mauersberger et al. 1986; Mills & Morris 2013; Krieger et al. 2017; Ginsburg et al. 2016), higher densities ($10^{3\text{--}5}$ cm^{-3} ; Zylka et al. 1992; Mills et al. 2018a), and broader line widths, on the ~ 10 pc scale ($\sim 20\text{--}30$ km s^{-1} ; Bally et al. 1987; Kauffmann et al. 2017), than typical clouds in the interstellar medium (ISM) of the Galactic disk. The velocities of CMZ clouds range from -250 to $+250$ km s^{-1} within the inner 1.5 of our Galactic center. The large velocity range of these clouds, wide velocity dispersions,

and line-of-sight confusion from multiple velocity components can make it difficult to place individual molecular clouds within the 3-dimensional context of the CMZ. Figure 1 shows the inner 100 pc of the Galactic center, where many of these dense molecular clouds are shown in red in this 3-color image. Recent efforts have been made to connect these individual clouds ($1\text{--}10$ pc) to the larger structures (~ 100 pc) in the Galactic center (Sofue 1995; Sawada et al. 2004; Molinari et al. 2011; Kruijssen et al. 2015; Henshaw et al. 2016).

The 3-dimensional orientation of the large-scale structures in the CMZ can depend greatly on the interpretation of the gas kinematics. For example, Sofue (1995) and Sawada et al. (2004) suggest a two spiral arm structure, whereas Molinari et al. (2011) argue for a twisted elliptical ring. The most recent orbital model, presented in Kruijssen et al. (2015), suggests an open orbit solu-

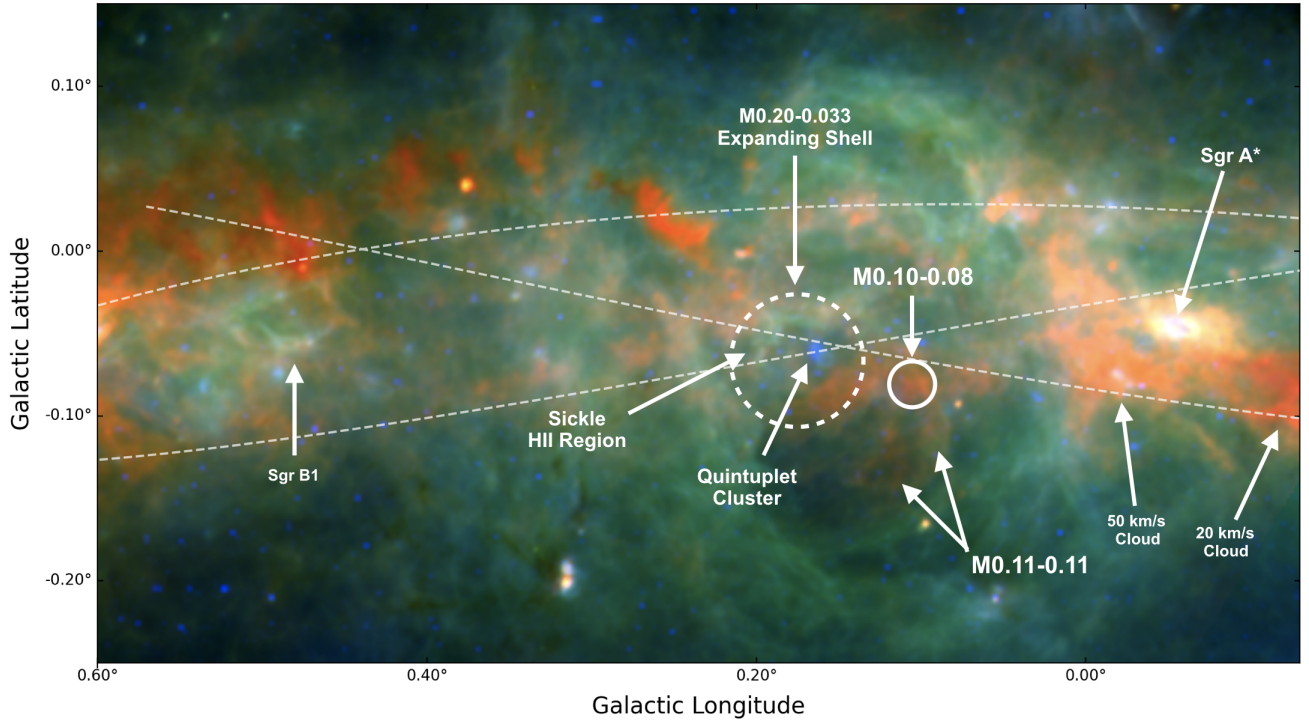


Figure 1. Three-color composite of the inner 100 pc of the CMZ, centered on the Radio Arc region, where red and green are the 160 and 70 μm emission, respectively, from HiGAL (Molinari et al. 2010), and blue is 8 μm emission from Spitzer (Churchwell et al. 2009). The solid white circle shows the region of the CMZ targeted in this study. This field is centered on the M0.10–0.08 molecular cloud, but could overlap with some of the extended emission in M0.11–0.11. The dashed white circle shows the location of the M0.20–0.033 expanding shell presented in Butterfield et al. (2018). Additional prominent CMZ regions are labeled for reference purposes. Overlaid on this figure is a dashed line showing the extent of the orbital stream proposed by Kruijssen et al. (2015).

tion (see dashed line in Figure 1 for the projected trajectory of their orbital model solution). In the Kruijssen et al. (2015) orbital model, gas in the CMZ traces an open orbit set by the shape of the CMZ potential. Connected chains of molecular clouds all follow the same orbital path or ‘stream’. The 3-dimensional arrangement of clouds along a continuous stream can be loosely reconstructed from their projected radial distance to Sgr A* and the observed line-of-sight velocity. However, there is still some ambiguity about whether certain features are located on the near or far sides of the Galactic center. Additionally, multiple components along the same line-of-sight can make it challenging to disentangle the kinematics of a single cloud. High spatial and spectral resolution observations targeting regions where the kinematics are complex are needed to resolve the individual components.

One region of the CMZ where the kinematics are complex is toward the M0.10–0.08 molecular cloud (solid white circle in Figure 1). The M0.10–0.08 cloud, and the adjacent M0.11–0.11 cloud (annotated in Figure 1), have been observed in several large-scale surveys of molecular gas in the CMZ for many decades (Güsten

et al. 1981; Tsuboi et al. 1997; Chuss et al. 2003; Handa et al. 2006; Jones et al. 2012; Mills & Battersby 2017; Battersby et al. 2020; Hatchfield et al. 2020; Guan et al. 2021). Several of the low-spatial-resolution surveys of cold dust and molecular gas show that the M0.10–0.08 cloud is relatively bright and compact (<3 pc), with a mass of $1.7 \times 10^5 M_{\odot}$ (e.g., Tsuboi et al. 2011). The M0.10–0.08 cloud also been observed to have substructure, as detected in the recent 1mm CMZoom survey (Battersby et al. 2020; Hatchfield et al. 2020). M0.11–0.11, however, is relatively faint and extended (>5 pc) and could spatially overlap with M0.10–0.08 (Figure 1). The spatial overlap between the two clouds has led some investigators to argue for a possible connection between the two clouds (Handa et al. 2006; Clavel et al. 2013). However, there are unsolved questions about this connection in the literature due to the large velocity separation between the two clouds along this line-of-sight ($\Delta v \sim 30 \text{ km s}^{-1}$; Ponti et al. 2010; Kruijssen et al. 2015). Understanding the connection or separation of the two clouds can give insight on the complex kinematics in the region. Furthermore, disentangling the complex kinematics into a some-

Table 1. Spectral Line Imaging Parameters for the 15 molecular transitions detected in this study

Species & Transition	Rest Frequency (GHz)	—Restoring Beam ^a —		Position Angle (°)	Velocity Resolution (km s ⁻¹)	rms per Channel (mJy beam ⁻¹)	Peak Intensity (mJy beam ⁻¹)
		Major Axis (″)	Minor Axis (″)				
NH ₃ (1,1)	23.69450	2.81	2.62	-81.85	1.58	1.3	57.6
NH ₃ (2,2)	23.72263	2.79	2.62	-85.45	1.58	1.4	56.3
NH ₃ (3,3)	23.87013	2.77	2.60	-85.18	3.14	2.3	485.9
HC ₅ N (9–8) ^{bc}	23.96390	3.00	3.00	0.00	3.13	0.8	6.4
NH ₃ (4,4)	24.13942	2.79	2.59	89.49	3.10	1.0	42.0
OCS (2–1) ^{bc}	24.32593	5.00	5.00	0.00	3.08	1.2	8.6
NH ₃ (5,5)	24.53299	2.74	2.55	-90.00	3.05	0.8	28.3
CH ₃ OH (6 ₂ –6 ₁) ^{bc}	25.01812	3.00	3.00	0.00	3.00	0.8	5.6
NH ₃ (6,6)	25.05603	2.63	2.48	89.48	2.99	0.9	29.4
NH ₃ (7,7)	25.71518	2.58	2.40	-83.33	2.91	0.7	11.8
HC ₃ N (3–2)	27.29429	3.14	2.52	16.76	2.75	2.2	55.2
NH ₃ (9,9) ^c	27.47794	2.80	2.45	43.30	2.73	2.0	16.8
CH ₃ OH (4 ₁ –3 ₀)	36.16927	1.95	1.81	-174.63	1.05	2.9 (50) ^d	46969.0
HC ₃ N (4–3)	36.39232	1.98	1.81	-3.02	2.06	2.8	47.0
CH ₃ CN (2–1) ^b	36.79547	3.00	3.00	0.00	1.02	4.3	40.7

^a Where 1″ is 0.04 pc at an assumed distance of 7.9 kpc to the CMZ (Do et al. 2019).

^b These four transitions were smoothed from the natural spatial resolution to improve the signal-to-noise.

^c These four transitions had a signal-to-noise ratio <9 and are therefore not shown in Figure 2.

^dThe larger value in parentheses is the rms noise in the channel containing the brightest maser, at $v = 50.6$ km s⁻¹.

what simple solution is essential for understanding the 3-dimensional structure of the gas and the effects that cloud-cloud interactions can have on the gas motions.

We present high-resolution (~ 2 – 3 ″) radio observations of M0.10–0.08 using the National Science Foundation’s Karl G. Jansky Very Large Array (hereafter, VLA). Using these observations we analyze the morphological and kinematic structure of M0.10–0.08 at high-resolution (Section 3) and discuss the relationship of M0.10–0.08 to other clouds in the region (Section 4).

2. OBSERVATIONS AND DATA CALIBRATION

The observations presented in this paper were taken with the VLA interferometric radio telescope, operated by the National Radio Astronomy Observatory.¹ These VLA observations were part of a larger survey of molecular clouds in the CMZ (PI: Elisabeth A.C. Mills; Project code: 11B-210).² This survey used the K (18.0–26.5 GHz) and Ka (26.5–40.0 GHz) band receivers on 2012 January 14th & 13th, respectively, with

the DnC hybrid array. In this survey we observed 15 spectral lines from several regions in the CMZ. The image cube parameters for all 15 lines are reported in Table 1. The results presented in this paper focus on a single pointing containing M0.10–0.08,³ centered at $\alpha(2000)=17^{\text{h}}46^{\text{m}}09^{\text{s}}.79$, $\delta(2000)=-28^{\circ}53'18''.0$, for K band, and $\alpha(2000)=17^{\text{h}}46^{\text{m}}11^{\text{s}}.37$, $\delta(2000)=-28^{\circ}53'24''.3$, for Ka band, with a time-on-source of ~ 25 minutes in each frequency band.

The correlator setup for this survey is described in Mills et al. (2015) and Butterfield et al. (2018). High-frequency VLA procedures⁴ were used for calibration and imaging, as described in Mills et al. (2015), with one difference. We employed the CLEAN parameter “multiscale” for all spectral lines that had a signal-to-noise ratio >15 and a peak intensity >20 mJy beam⁻¹ (see Table 1) in order to improve our sensitivity to data taken with short baselines in our interferometric observations.

³ All J<7 NH₃ images, shown in Figure 2, are from a larger multi-pointing mosaic (See Figure 3, left, in Butterfield et al. 2018).

⁴ [Hyperlink to the high frequency CASA tutorial](#). All imaging and calibration of the VLA observations presented here used the Common Astronomy Software Application (CASA) program provided by NRAO (McMullin et al. 2007).

¹ The National Radio Astronomy Observatory is a facility of the National Science Foundation operated under cooperative agreement by Associated Universities, Inc.

² Results from this survey have also been presented in: Mills & Morris (2013); Mills et al. (2014, 2015); Ludovici et al. (2016); Butterfield et al. (2018); Mills et al. (2018b).

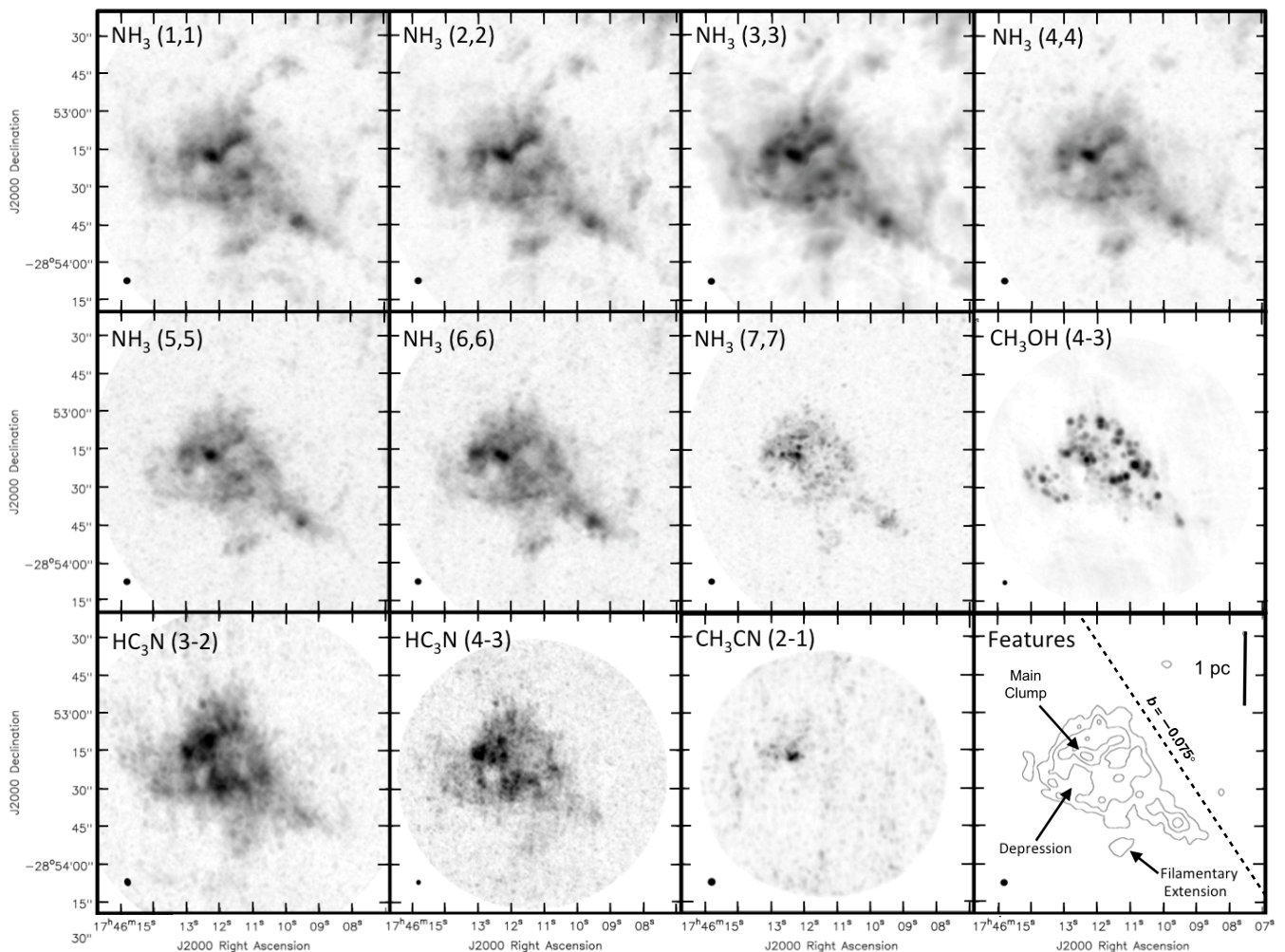


Figure 2. Peak intensity distribution of 11 of the 15 molecular line transitions detected in this paper. The top two rows show the NH_3 (1,1) – (7,7) and CH_3OH line emission. The bottom row shows the observed HC_3N and CH_3CN transitions. The bottom right-most panel shows the 20, 40, 80, and 140 σ contour levels of the NH_3 (3,3) emission, with annotations identifying several of the ‘Features’ discussed in Section 3.1.1. The spatial resolution of each presented molecular transition is shown in the bottom left corner of every panel. The imaging parameters of all 15 detected molecular transitions are described in Table 1. The black dashed line shows the orientation of the Galactic plane at $b = -0^\circ 075$.

3. RESULTS

3.1. Morphology of the Molecular Emission in $M0.10-0.08$

Figure 2 presents the peak intensity emission of 11 molecular transitions detected in $M0.10-0.08$ (see Table 1 for imaging parameters). The remaining four detected molecular transitions in $M0.10-0.08$ are relatively faint ($<9\sigma$) and are therefore *not* shown in Figure 2. In the following sections we examine the bright, diffuse molecular emission (§3.1.1: NH_3 & HC_3N). We focus on the kinematics of the NH_3 emission and fit the averaged gas profile in Section 3.2. The CH_3OH (4_1-3_0) class I maser transition is discussed in detail in Section 3.3.

3.1.1. Morphology of the Diffuse Molecular Emission: NH_3 and HC_3N

The top two rows in Figure 2 show the detected NH_3 (1,1)–(7,7) emission in $M0.10-0.08$. The distribution of the metastable NH_3 emission is similar across all seven transitions. The speckled morphology observed in the NH_3 (7,7) transition is likely an artifact of cleaning with delta functions (see Section 2 and Table 1 for a discussion on the cleaning process).

Most of the NH_3 emission in the $M0.10-0.08$ cloud is concentrated within a square arcminute region near the center of the field. At high-resolution ($3''$) the $M0.10-0.08$ cloud has a wedge-like appearance that is narrow at lower Galactic longitude ($10''$; $l=0^\circ 095$) and widens with increasing Galactic longitude ($50''$; $l=0^\circ 11$).

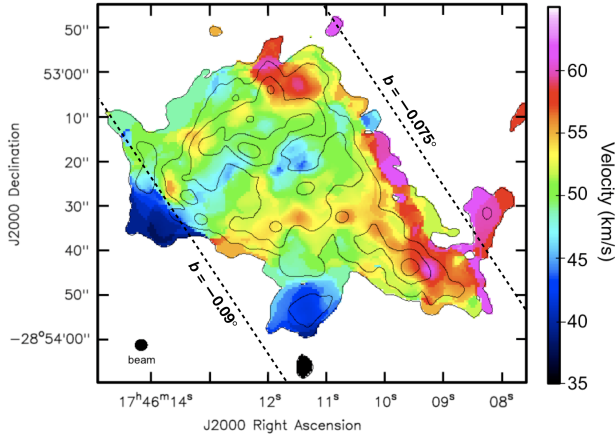


Figure 3. Intensity-weighted velocity distribution (1st moment map) of the NH_3 (3,3) transition for emission above the 10σ level, integrated over a velocity range of -20 – 100 km s^{-1} . The black contours correspond to emission at 10 , 20 , 40 , 80 , & 140×2.3 mJy beam^{-1} (rms level). The black dashed lines show the orientation of the Galactic plane at $b = -0.075$ and $b = -0.09$.

This wedge-like structure is also noticeable in both transitions of HC_3N : 3–2 and 4–3 (bottom row in Figure 2). Additionally, there is a diffuse ‘filamentary extension’ toward the southern region of M0.10–0.08, as indicated in the bottom right-most panel of Figure 2 (i.e., ‘Features’ panel). This filamentary extension is detected in both the NH_3 and HC_3N transitions, but not in the CH_3OH (4–3) transition. The longest extent of M0.10–0.08 is $75''$ (~ 3 pc), indicating that this cloud is among the more compact of molecular clouds observed in the Galactic center (diameters of 3–10 pc; e.g., Güsten et al. 1981; Bally et al. 1987; Kauffmann et al. 2017; Mills & Battersby 2017).

Within M0.10–0.08 there are several (~ 5) compact clumps ($D < 10''$) of brighter NH_3 emission (> 0.2 Jy beam^{-1}) that are most prominent in the (3,3) transition. Most of these compact clumps are concentrated toward the northeast region of the cloud, with the brightest NH_3 clump located at: $\alpha(2000) = 17^{\text{h}}46^{\text{m}}12^{\text{s}}.3$, $\delta(2000) = -28^{\circ}53'18''$. The brightest clump (i.e., ‘Main Clump’; see ‘Features’ panel in Figure 2) contains emission in all 11 transitions shown in Figure 2, including the fainter CH_3CN (2–1) transition. Further, the Main Clump is the only location where we detect CH_3CN emission. Directly south of the Main Clump is a lower intensity emission region (‘Depression,’ labeled in the Features panel of Figure 2). This depression region is $\sim 10''$ across and is located at $\alpha(2000) = 17^{\text{h}}46^{\text{m}}12^{\text{s}}.5$, $\delta(2000) = -28^{\circ}53'25''$. The Depression is detected in both NH_3 and HC_3N , but

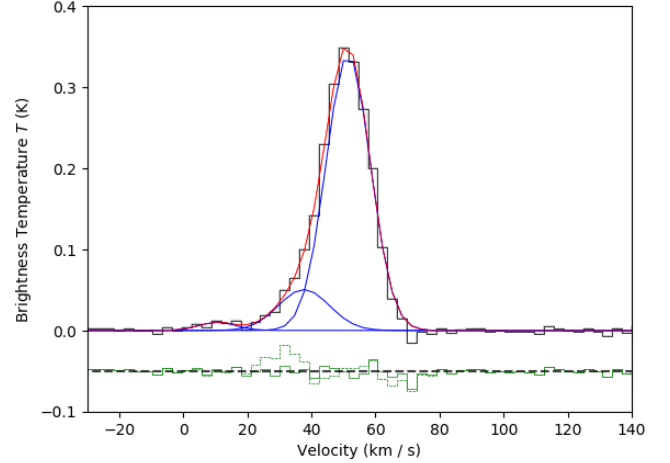


Figure 4. NH_3 (5,5) velocity spectrum averaged over the entire field of view. The NH_3 (5,5) line was chosen as a representative spectrum to show the multiple components toward this region. In the (5,5) line all three components are detected and at this higher J transition, the hyperfine lines are suppressed. The black line shows the data. The blue Gaussians show the individual components (presented in Table 2), with the red line showing the sum of the three Gaussian components. The solid green line at -0.05 K shows the residuals of the three-Gaussian-component fit. The dashed green line at -0.05 K shows the residuals of a two-Gaussian-component fit ($v_c \simeq 10$ km s^{-1} and 50 km s^{-1}). In the two Gaussian fit there is consistent excess of emission around ~ 20 – 40 km s^{-1} (six spectral cube channels; dashed green line). This excess emission around 20 – 40 km s^{-1} is brighter than the emission in the 10.6 km s^{-1} component and is detected in the HC_3N transitions as well. Therefore, we interpret the excess emission as an intermediate-velocity component.

is most prominent in the HC_3N (4–3) transition.⁵ Although this feature is detected in all of our extended emission lines (NH_3 , HC_3N), it could be produced by spatial filtering in our interferometer data. Future observations at different wavelengths are necessary to determine whether the Depression is some kind of cavity.

3.2. Kinematics of the NH_3 Emission

Figure 3 shows the centroid velocity distribution (moment 1) of the NH_3 (3,3) transition. Most of the bright NH_3 emission ($> 10\sigma$) is at a velocity of 35 – 65 km s^{-1} . However, as we will show in the following section, faint ($< 10\sigma$) molecular emission is detected at lower velocities of ~ 10 km s^{-1} .

⁵ There is a second lower level emission region to the west of the Main Clump and north of the Filamentary Extension (see Figure 2). However, because we detect emission above the noise level in this region in the HC_3N (4–3) transition, we do not characterize this feature as a second ‘depression’.

Table 2. Kinematics of the NH₃ (5,5) transition

Parameter ^a	Value
Low Velocity Component	
v_c	$10.6 \pm 2.5 \text{ km s}^{-1}$
σ	$5.8 \pm 2.6 \text{ km s}^{-1}$
T_B	$0.01 \pm 0.003 \text{ K}$
Intermediate Velocity Component	
v_c	$37.6 \pm 5.7 \text{ km s}^{-1}$
σ	$8.0 \pm 3.0 \text{ km s}^{-1}$
T_B	$0.05 \pm 0.02 \text{ K}$
High Velocity Component	
v_c	$51.5 \pm 0.6 \text{ km s}^{-1}$
σ	$6.9 \pm 0.3 \text{ km s}^{-1}$
T_B	$0.34 \pm 0.03 \text{ K}$

^a v_c is the central velocity of the component, σ is the velocity dispersion and T_B is the peak brightness temperature.

We note an asymmetry in the velocity distribution that results in roughly a $10 \text{ km s}^{-1} \text{ pc}^{-1}$ gradient (where 1 pc is $\sim 25''$). Most of the higher-velocity NH₃ (3,3) emission ($v \geq 55 \text{ km s}^{-1}$) is located toward the north-western side of M0.10–0.08 (around $b = -0^\circ 075$) and the lower-velocity emission ($v \leq 45 \text{ km s}^{-1}$) is generally located toward the south and south-eastern sides of M0.10–0.08 (around $b = -0^\circ 09$). The orientation of the described velocity gradient is perpendicular to the direction of orbital motion in the Kruijssen et al. (2015) orbital model. The filamentary extension, described in Section 3.1, contains mainly lower velocity emission ($35\text{--}45 \text{ km s}^{-1}$) and is oriented roughly parallel to the described velocity gradient.

3.2.1. Multiple velocity components toward M0.10–0.08

Moment 1 maps, like the one presented in Figure 3, have the advantage of showing the predominant velocity distribution across a cloud or region. However, these maps can be misleading since they can average over multiple components and be weighted by the brighter emission components. Integrating the emission across a cloud or region, and analyzing the spectra using fitting programs like *pyspeckit* (Ginsburg & Mirocha 2011; Ginsburg et al. 2022)⁶ can help identify and distinguish multiple components. Once these velocity components are disentangled we can map their spatial distribution and morphology by isolating channels associated with the individual velocity component. By analyzing the gas kinematics using numerous methods we can under-

⁶ The *pyspeckit* python program is available online at <https://github.com/pyspeckit/pyspeckit>.

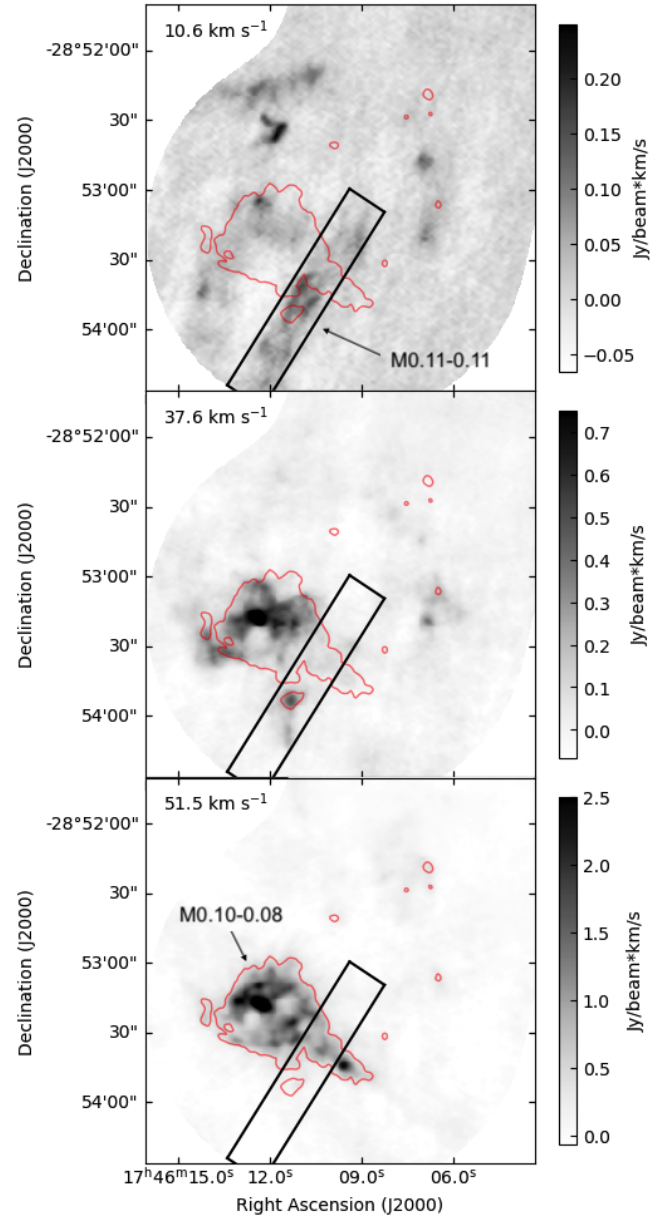


Figure 5. Molecular morphology of the three velocity components presented in Table 2 (integrated intensity, moment 0, in NH₃ (3,3)). These panels were made using $V_c \pm \sigma_v$ (to the closest channel). The red contour in all three panels shows the 20σ level from the ‘Features’ panel in Figure 2 for spatial reference. Annotated on the 10.6 and the 51.5 km s^{-1} panels are the M0.11–0.11 and M0.10–0.08 clouds, respectively. The black box shows the region used for the position-velocity slice in Figure 7.

stand the relative structure of the two clouds towards this complex region. In this section we will identify the velocity components towards the M0.10–0.08 cloud by analyzing the NH₃ (5,5) line.

Figure 4 shows the raw integrated spectrum (black histogram) of the NH_3 (5,5) line. We chose to analyze the $J=5$ NH_3 transition because the hyperfine satellite lines are quite weak and do not contribute significantly to the spectrum. We initially fit the NH_3 (5,5) line with two main Gaussian components at $\sim 10\text{--}15$ km s^{-1} and $\sim 50\text{--}55$ km s^{-1} . The residuals from this initial fit showed an excess around $20\text{--}40$ km s^{-1} (dashed green line; Figure 4). This excess emission, which appears as a lower-velocity wing to the brighter $\sim 50\text{--}55$ km s^{-1} velocity component, is detected in nearly all of our observed lines (e.g., NH_3 , HC_3N). Since this excess is detected in multiple molecules and transitions, we interpret it to be an intermediate velocity component. Including a third component in our fitting process greatly reduced the residuals to produce the solid green residual in Figure 4. The final fit parameters used to produce the three Gaussian components in Figure 4 are listed in Table 2.

The lowest velocity component, which has a central velocity of 10.6 km s^{-1} , is the faintest of the three components. This velocity component is detected in both the HC_3N transitions and in the NH_3 lower J -transitions ($J < 7$). The highest velocity component, fit with a central velocity of 51.5 km s^{-1} , is the brightest of the three components and is detected in all of our observed molecular lines. This velocity component appears to dominate the moment 1 map, shown in Figure 3. The intermediate velocity component, which is best fit with a central velocity of 37.6 km s^{-1} in the NH_3 (5,5) line, is shown to be slightly spatially offset from the high velocity component in Figure 3. We note that, while present, the central velocity of the intermediate velocity component did vary between the different molecular transitions, ranging from $\sim 30\text{--}45$ km s^{-1} . Therefore, the error estimates on the central velocity of the intermediate component are much larger than those shown in the Low and High velocity components to reflect this uncertainty.

We can further analyze the morphology of the molecular emission by isolating the channels associated with each component. Figure 5 shows the distribution of the NH_3 (3,3) emission in each velocity component, labeled by their respective central velocities from Table 2. We are using the NH_3 (3,3) line for this analysis due to the faintness of the low-velocity component in the NH_3 (5,5) transition. When integrating over the field we were sensitive enough to detect the 10.6 km s^{-1} component, but for a spatial mapping the NH_3 (5,5) line is not bright enough to perform a pixel by pixel analysis of that component. We are aware that the hyperfine satellite lines of the NH_3 (3,3) emission will be more prominent than

in the (5,5) transition and will acknowledge where those lines may contribute in the following discussion.

In general, the observed gas morphology is unique for each velocity component. The 51.5 km s^{-1} velocity gas is concentrated toward the center of the field and closely follows the bright NH_3 emission in Figure 2, with the exception of the filamentary extension (e.g., see the wedge-shaped distribution in the red contour, Figure 5). The 10.6 km s^{-1} component is distributed throughout the field-of-view and contains several elongated structures (e.g., black box in Figure 5). Further, this component does not appear to have similar morphology with the 51.5 km s^{-1} component, suggesting this gas could be independent from the 51.5 km s^{-1} emission. The morphology of the 37.6 km s^{-1} component has similar attributes to both the 10.6 and 51.5 km s^{-1} components. Unlike the 51.5 km s^{-1} component, the 37.6 km s^{-1} component *is* associated with the filamentary extension. Further, the filamentary extension closely follows the elongated structure in the 10.6 km s^{-1} component (Figure 5). The 37.6 km s^{-1} component also contains concentrated emission toward the north which spatially overlaps with emission in the 51.5 km s^{-1} component. Because of this spatial overlap, some of the 37.6 km s^{-1} emission could be from the hyperfine lines in the 51.5 km s^{-1} component.

3.3. 36.2 GHz CH_3OH Masers in M0.10–0.08

Our Ka-band observations included the 36.2 GHz CH_3OH ($4_{-1}\text{--}3_0$) maser transition. This class I maser is known to trace shocks, as it is collisionally excited (Morimoto et al. 1985; Menten 1991; Sjouwerman et al. 2010). The 36.2 GHz CH_3OH ($4_{-1}\text{--}3_0$) maser transition has previously been detected towards this region (Yusef-Zadeh et al. 2013; Cotton & Yusef-Zadeh 2016). Our data suggest there are at least one hundred compact CH_3OH sources in M0.10–0.08 (Figure 2, second row, last panel). The compact CH_3OH sources in M0.10–0.08 are located within a square arcminute region, and closely follow the bulk of the NH_3 and HC_3N emission at velocities from $40\text{--}60$ km s^{-1} (Figure 5, bottom panel).

Figure 6 shows the spatial distribution (left) and the velocity distribution (right) of the bright, above 0.6 Jy beam^{-1} (12σ), 36.2 GHz CH_3OH emission. The CH_3OH emission is not uniformly distributed throughout M0.10–0.08. Most of the CH_3OH emission appears to be distributed throughout the wedge-like structure (discussed in Section 3.1.1). We do not detect any compact emission, above 12σ , from the filamentary extension (e.g., see Figures 2 and 6).

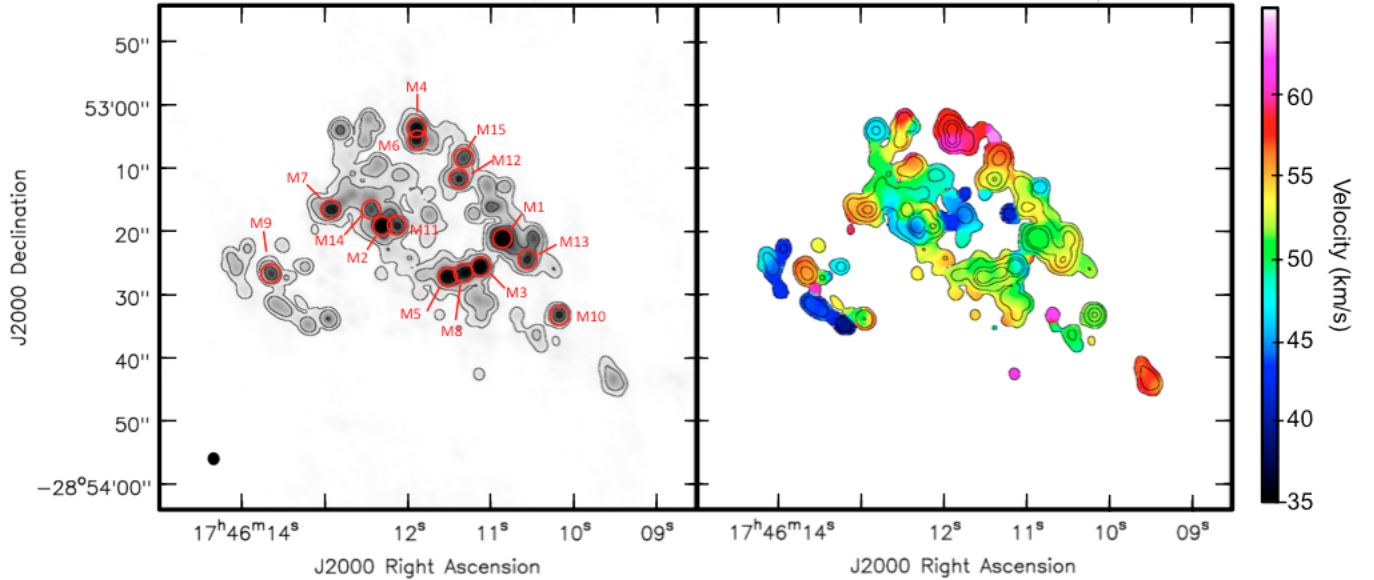


Figure 6. Distribution of the 36.2 GHz CH_3OH (4_1-3_0) masers in M0.10–0.08 showing the maximum intensity emission (*left*), from Figure 2, and central velocities (*right*) for emission above the 12σ level. The overlaid contours show 12, 30, 100, and $200 \times 50 \text{ mJy b}^{-1}$ (rms noise in brightest channel). The 15 brightest masers from Table A.1 are marked on the *left* panel.

The velocity of the CH_3OH emission in M0.10–0.08 ranges from ~ 35 to 65 km s^{-1} . This corresponds to the velocity range of the bright NH_3 emission (Figure 3). This velocity range indicates that most of the CH_3OH maser emission is associated with the 37.6 and 51.5 km s^{-1} velocity components.

In order to characterize the nature of the point-like emission and to evaluate whether these detections represent maser emission, we used the source detection algorithm, *Clumpfind* (Williams et al. 1994), to distinguish the emission both spectrally and spatially. *Clumpfind* identifies local maxima and uses saddle-points in position and velocity space around the local maxima to determine the boundaries of the sources. *Clumpfind* then produces a list of clumps with uniform criteria, which was used to construct a catalog (for more details on maser identification using the *Clumpfind* algorithm, see the description of this technique in Mills et al. 2015, Section 5.1). Sixty-four of the compact CH_3OH sources have brightness temperatures over 400 K (i.e., ‘ CH_3OH masers’). The properties of the 64 detected ‘ CH_3OH masers’ identified with *Clumpfind* are listed in Table A.1. The spectral profiles of these masers are shown in Figure A.1. The 15 brightest masers in M0.10–0.08 are labeled in Figure 6 (left).

With *Clumpfind* we also detect 31 compact CH_3OH sources that have a brightness temperature between 100 – 400 K , which we regard as ‘maser candidates.’ These sources are considered to be candidate masers based on their brightness temperature, which are similar

to observed gas temperatures in CMZ clouds (50 – 400 K , Mills & Morris 2013; Krieger et al. 2017). Therefore, we assume that any emission above this upper 400 K limit is likely non-thermal (i.e., maser emission, sources in Table A.1) and any emission that is below 100 K is most likely thermal. Therefore, we classify CH_3OH point-sources that have brightness temperatures between 100 – 400 K as ‘maser candidates’. The properties of all 31 maser candidates are listed in Table A.2, with their spectra shown in Figure A.2. These maser candidates are also located within the same square arcminute region as the detected CH_3OH masers and have a similar velocity range (41 – 63 km s^{-1}).

4. DISCUSSION

In the following section we present a discussion and interpretation of our kinematics results on the M0.10–0.08 cloud (Section 3). Here, we attempt to explain the complicated and multiple-component velocity structure detected in the vicinity of M0.10–0.08 (Sections 4.1 & 4.2).

4.1. Locations and Origins of M0.10–0.08 and M0.11–0.11

The bulk emission in this region of the Galactic center has a velocity around 51.5 km s^{-1} (Section 3.2.1). The morphology and gas kinematics of this velocity component are consistent with those found in previous studies of M0.10–0.08 (e.g., Tsuboi et al. 2011). M0.10–0.08 appears to be part of a larger structure of molecular gas that has a velocity of around 50 km

s^{-1} (Fukui et al. 1977; Tsuboi et al. 2011). Tsuboi et al. (2011) detected H^{13}CO^+ emission around 50 km s^{-1} extending from $+0.15^\circ$ to -0.05° ($d \sim 27 \text{ pc}$; see their Figure 10). Within this extended diffuse structure they detect three concentrated regions of H^{13}CO^+ emission that coincide with the M0.10–0.08, M0.07–0.07, and 50 km s^{-1} cloud (M–0.02–0.07) molecular clouds (see Figure 1 for locations of these clouds). The presence of all three clouds within this larger diffuse structure could be evidence that all three clouds are co-located within a single lower-density envelope that has a velocity of around 50 km s^{-1} .

This large diffuse gas structure, observed in H^{13}CO^+ by Tsuboi et al. (2011), may be Orbital Stream 1 in the Kruijssen et al. (2015) orbital model. The 50 km s^{-1} cloud is argued to be associated with Orbital Stream 1 (Kruijssen et al. 2015). Therefore, if M0.10–0.08 and M–0.02–0.07 are associated within the same gas stream, and 50 km s^{-1} cloud is located on Orbital Stream 1, then by extension we can infer that M0.10–0.08 is also located on Orbital Stream 1. We note, however, that in the Kruijssen et al. (2015) orbital stream model, gas at the closest angular location to the M0.10–0.08 cloud ($l = 0^\circ 09$, $b = -0^\circ 07$; as the position of M0.10–0.08 is slightly offset from Orbital Stream 1 by $\sim 1'$) is predicted to have a line-of-sight velocity of 60 to 65 km s^{-1} . Although this suggested line-of-sight velocity is slightly higher than the central velocity of M0.10–0.08 that we measured in Figure 4, we do detect some gas at velocities of around 60 to 65 km s^{-1} (see Figures 3 & 6, right).

The M0.20–0.033 expanding shell is also hypothesized to be located on Orbital Stream 1 (Butterfield et al. 2018, see our Figure 1 for spatial location of shell relative to other GC clouds). In Butterfield et al. (2018) we reported a systemic velocity of $\sim 53 \text{ km s}^{-1}$ for the M0.20–0.033 expanding shell and advocate that the shell is also located on Orbital Stream 1, based on position-velocity analysis. Indeed, the adjacent locations of M0.10–0.08 and the M0.20–0.033 expanding shell (see Figure 1) and their similar velocities are consistent with both clouds being on the same orbital stream. Additionally, based on the orbital direction of stream 1, the M0.10–0.08 cloud would be located ‘upstream’ from the M0.20–0.033 expanding shell. Based on the orbital solution in Kruijssen et al. (2015), M0.10–0.08 would orbit into the current location of the M0.20–0.033 expanding shell in ~ 0.05 Myrs.

The 10.6 km s^{-1} component (Figure 4; Section 3.2) covers a velocity range of ~ 0 – 20 km s^{-1} based on analysis of the NH_3 (5,5) emission and additional analysis of the HC_3N lines. This velocity range is similar to

observed velocities of the adjacent M0.11–0.11 molecular cloud (~ 10 – 30 km s^{-1} ; Jones et al. 2012; Clavel et al. 2013, see their Figure 2), and nearby gas velocities associated with with Kruijssen et al. (2015) orbital stream 3 (~ 0 – 5 km s^{-1}). However, there are discrepancies in the literature concerning the velocity of the M0.11–0.11 cloud. Tsuboi et al. (1997), Handa et al. (2006), and Tsuboi et al. (2011) report a slightly higher velocity range of 15 – 45 km s^{-1} . These velocity values of the M0.11–0.11 cloud in Tsuboi et al. (1997), Handa et al. (2006), and Tsuboi et al. (2011) are closer to those of the intermediate velocity component in our observations (37.6 km s^{-1} ; see Section 3.2.1). In our Figure 4 this velocity component appears as a lower velocity ‘wing’ of the main 51.5 km s^{-1} component, rather than a distinct cloud. Further, the morphology of the 37.6 km s^{-1} component in Figure 5 appears to overlap with the 51.5 km s^{-1} component with the exception of the filamentary extension. Therefore, based on the previous work of Jones et al. (2012) and Clavel et al. (2013) and our analysis above, we interpret the 10.6 km s^{-1} component as extended emission associated with M0.11–0.11.

4.1.1. *Similar X-ray fluorescence detected in both M0.10–0.08 and M0.11–0.11*

Observed X-ray fluorescence can be beneficial in determining radial distances, which, when combined with their projected separation from the Galactic center, can be used to infer inter-cloud distances (e.g., Clavel et al. 2013; Terrier et al. 2018). In our Galactic center, fluorescent iron emission at 6.4 keV is created in molecular clouds by K-shell photo-ionization and Compton scattering of neutral iron atoms from a previous, gigantic X-ray flare, presumably from Sgr A*. By observing the time delay of the detected X-ray reflection across multiple molecular clouds, we can constrain the locations of clouds from the geometrical path-length between the clouds and Sgr A* and determine their location along our line-of-sight (e.g., Cramphorn & Sunyaev 2002). Further, the time delay between the detected reflections provides a measurement of the total path traveled by the photons, assuming they were emitted simultaneously. This path length then gives an indication of the relative locations of the clouds.

Molecular clouds that show similar illumination at a similar timeframe are located along the same 3-dimensional ‘parabola’, assuming the illumination feature is produced by the same, single flaring event (e.g., Sunyaev & Churazov 1998). Along this 3-dimensional parabola, the path length of the propagating light signal (from Sgr A* to the cloud and then to the Earth) is the same at each location and therefore the time delay of the propagating signal is the same as well. Clavel et al.

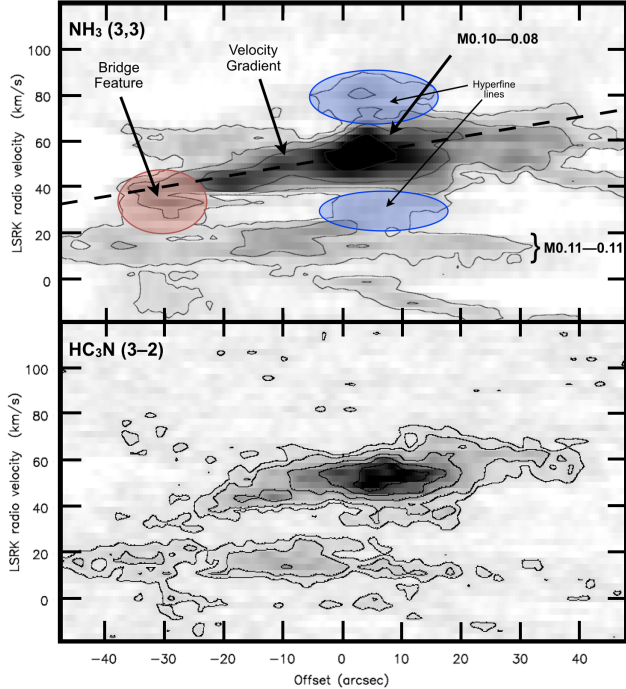


Figure 7. Position-velocity distribution across the spatial slice shown in Figure 5, for NH_3 (3,3) (top) and HC_3N (3-2) (bottom). Annotations in the top panel show the gas associated with M0.11-0.11 and M0.10-0.08 (see Section 4.1). The black dashed line shows the magnitude and orientation of the $\sim 10 \text{ km s}^{-1} \text{ pc}^{-1}$ velocity gradient described in Section 3.2. The blue regions in the top panel show the general locations of the hyperfine satellite lines ($\pm 20\text{--}30 \text{ km s}^{-1}$ from the main component) of M0.10-0.08. The red shaded region highlights the ‘bridge’-like feature discussed in Section 4.2.

(2013) detected a similar X-ray fluorescence signature in both M0.10-0.08 and M0.11-0.11 (sources Br2 and G0.11-011 in their study).⁷ This detection of similar X-ray fluorescence illumination in M0.10-0.08 and M0.11-0.11 indicates the two clouds are located along the same 3-dimensional parabola, assuming the fluorescence in both clouds is from the same event. Further, because the two clouds are aligned along the same line of sight, and have a similar X-ray fluorescence light curve, Clavel et al. (2013) argue the two clouds must be at the same physical position, even with their differences in velocity. If the two clouds are almost at the same physical location, then we would expect to see evidence of this interaction.

⁷ The data presented in Clavel et al. (2013) used Chandra observations from 1999 to 2011 (see their Table 1 for observational information). These X-ray observations had a resolution of $4''$, and are therefore fairly comparable to the observations presented in this paper, Table 1.

4.2. Proposed Physical Interaction between M0.10-0.08 and M0.11-0.11

Previous studies have hinted at a possible connection between M0.10-0.08 and M0.11-0.11 (Handa et al. 2006; Clavel et al. 2013). However, because of the large velocity difference between the two clouds along this line-of-sight ($\Delta v \sim 30 \text{ km s}^{-1}$), other investigators have suggested these components are physically separated (Ponti et al. 2010; Kruijssen et al. 2015). The high-resolution data presented in this paper can provide insight into this discrepancy in the literature. In this section we perform a detailed position-velocity analysis on this region to investigate a possible connection between M0.10-0.08 and M0.11-0.11.

Figure 7 shows the position-velocity distribution of NH_3 (3,3) (top) and HC_3N (3-2) (bottom) across the filamentary extension (black box in Figure 5). This slice was selected to maximize the relatively faint signal of the M0.11-0.11 cloud (top panel in Figure 5) and illustrate a possible connection to M0.10-0.08. The slice contains emission in all three velocity components (Table 2 and Figure 5). Emission associated with the M0.10-0.08 cloud is clearly the brightest component in this region ($50\text{--}60 \text{ km s}^{-1}$), with possible hyperfine lines above and below the main emission region (blue shaded region in Figure 7, top). These hyperfine lines have a fixed known separation from the main component of $\pm 21.1 \text{ km s}^{-1}$ and $\pm 29.1 \text{ km s}^{-1}$ for the NH_3 (3,3) transition (e.g., Krieger et al. 2017). The NH_3 emission at $\sim 80 \text{ km s}^{-1}$ is not observed in HC_3N (3-2) (Figure 7, bottom), suggesting it is hyperfine line emission. Across this slice there is clear, extended emission in M0.11-0.11 (10.6 km s^{-1} component; Figure 7, top). The emission in M0.11-0.11 is relatively faint compared to M0.10-0.08 and spans a velocity range from 5 to 25 km s^{-1} .

The 37.6 km s^{-1} component appears as a lower velocity wing to the 51.5 km s^{-1} component in the integrated spectrum (Figure 4). When isolating velocity channels associated with each component we see that some of the gas in the 37.6 km s^{-1} component is spatially offset from the 51.5 km s^{-1} component (Figure 5). We also observe this offset in position-velocity space, where some of the gas in the 37.6 km s^{-1} component appears to be spatially offset from the bulk of the 51.5 km s^{-1} component (Figure 7, top). Additionally, the 37.6 km s^{-1} component is mainly associated with emission along the velocity gradient (see Section 3.2) and appears to be a distinct feature in position-velocity space. Further, at the southern edge of the velocity gradient there is a bridge feature with emission between velocities $20\text{--}40 \text{ km s}^{-1}$ (red shaded region in Figure 7, top). Including

both the bridge feature and the velocity gradient results in continuous emission between 20–50 km s⁻¹, thereby showing that M0.10–0.08 and M0.11–0.11 have an apparent connection in position-velocity space. Analysis of the HC₃N (3–2) line shows a similar velocity gradient and bridge-like features across the slice (Figure 7, bottom). However, the HC₃N emission is $\sim 5\text{--}10\times$ fainter than the NH₃ (3,3) line, so these features appear loosely connected and barely above the noise level.

Recent studies simulating Galactic cloud-cloud interactions predict broad ‘bridge’-like feature in position-velocity space, where the two clouds are physically connected (e.g., Takahira et al. 2014; Haworth et al. 2015; Torii et al. 2017).⁸ In these studies, there is intermediate-velocity gas between the two main cloud components, which produces the ‘bridge’ in position-velocity space. Such bridge features have since been detected in numerous molecular clouds throughout the galaxy (e.g., Fukui et al. 2016; Torii et al. 2017).

Large-scale observations ($\sim 45''$ resolution) of the intermediate velocity component (15–45 km s⁻¹) from Tsuboi et al. (1997) and Handa et al. (2006) show the gas is extended and dense. Tsuboi et al. (1997) extracted a position-velocity slice at $b = -6'$ ($4' \leq l \leq 14'$) from their CS data cubes and observed two vertical features in velocity space that spanned 15 km s⁻¹ to 40 km s⁻¹, and were separated by $\sim 2'$ (see their Figure 2). Handa et al. (2006) also saw similar vertical features in velocity space in their H¹³CO⁺ and SiO data cubes. Tsuboi et al. (1997) attribute the vertical velocity features to be an expanding shell centered on a lower emission region near the centroid of the cloud, where the bright vertical features are the limb brightened edges of the shell. However, these vertical features could alternatively be signatures of the bridge feature, discussed above, on larger scales. At the low spatial resolution of the Handa et al. (2006) and Tsuboi et al. (1997) observations ($\sim 45''$), the detailed substructure we observed at $-45''$ to $0''$ in Figure 7 (top) would blend into a single pixel. Therefore the high-resolution gradient and bridge features shown in Figure 7 would appear as broad, continuous emission at $45''$ resolution.

Thus, based on the close physical proximity of M0.10–0.08 and M0.11–0.11 from X-ray fluorescence data, along with continuous emission connecting them in position-velocity space via a ‘bridge’ feature, we argue

⁸ This labeling of the ‘bridge’-like feature in position-velocity space, defined in Haworth et al. (2015), should not be confused with the X-ray definition of the Bridge, labeled as Br1 and Br2 (Ponti et al. 2010; Clavel et al. 2013), which spatially connects M–0.02–0.07 to M0.10–0.08.

the two clouds are physical interacting. Furthermore, this would imply that M0.11–0.11 is located on the same stream as M0.10–0.08 and not on a separate stream as indicated by the Kruijssen et al. (2015) orbital model.

4.3. Gas Kinematics in CMZ Clouds

Disentangling the molecular gas kinematics in CMZ clouds can be complex. As we have shown in this paper, the multiple velocity components toward the M0.10–0.08 cloud can make isolating the individual components challenging. For example, extensive efforts were conducted to fit the three components, with similar Gaussian fit parameters (V_c & σ), across multiple NH₃ transitions. However, we were unable to get converging values that satisfied the multiple transitions. The lower J transitions had brighter hyperfine structure for each component resulting in over nine blended profiles within the $\sim 0\text{--}70$ km s⁻¹ velocity range which could be fit with numerous solutions. At the higher J transitions, the 10.6 km s⁻¹ component was not bright enough to fit the spectrum.

The 37.6 km s⁻¹ component was also especially challenging to fit. Since this component appears as a low-velocity wing to the 51.5 km s⁻¹ component, there were numerous solutions to the profile that varied depending on the initial guesses and range limits in the *pyspeckit* program, with central velocity values that ranged from $\sim 30\text{--}45$ km s⁻¹. However, the presence of an intermediate velocity component between $\sim 30\text{--}45$ km s⁻¹ was clear in all of our NH₃ and HC₃N transitions (illustrated by the dashed green residuals in Figure 4). The fit solution we present in this paper (see Table 2) was the best fit parameters that accurately reflected the uncertainty in the 37.6 km s⁻¹ component. However, we note that determining a simple kinematic solution to complex kinematics in the CMZ can be problematic and requires multiple methods to disentangle the velocity components (i.e., spectral fitting, position-velocity analysis, moment images of components, etc).

Furthermore, the complex kinematics in the CMZ can make understanding the gas flows and unusual orbits more challenging. We have attempted to disentangle the kinematics towards this complicated region using high spatial and spectral resolution observations. While we were able to identify the three velocity components towards this region using a variety of methods, providing a simple solution that satisfies the kinematics observed in this dataset is more difficult. Future observations of complex kinematic regions should use a variety of methods to isolate the velocity components. If possible, future observations should also use absorption observations toward radio continuum regions to constrain the

line-of-sight arrangement, similar to the approach we used in [Butterfield et al. \(2018\)](#). Despite the complexity of disentangling the kinematics of multiple components, the analysis is necessary to constrain models of the large-scale gas structures. Models for the 3-dimensional orientations of these gas structures can be influenced by assumptions made in complex kinematic regions. Therefore, applying the solutions in complex kinematic regions in the models may help resolve some of the contingencies in future orbital solutions.

5. SUMMARY

We present high-resolution ($\sim 3''$) VLA radio observations of the compact (3 pc) M0.10–0.08 molecular cloud, finding that it is composed of multiple compact molecular clumps (5+ clumps; $D_{clumps} \leq 0.4$ pc; Section 3.1). We detect 15 molecular transitions in M0.10–0.08 (Table 1); including eight transitions of NH_3 , two HC_3N transitions, OCS, CH_3CN , HC_5N , and abundant 36.2 GHz CH_3OH masers (see Section 3.3 and Appendix A for details on the detected masers).

The main focus of this paper is on the molecular gas kinematics toward M0.10–0.08. We present the following results from this study:

1) Three velocity components detected toward M0.10–0.08: The averaged NH_3 (5,5) spectrum reveals three velocity components centered at 10.6, 37.6, and 51.5 km s^{-1} (see Section 3.2.1, Figures 4 & 5, and Table 2). Initially, the NH_3 (5,5) spectrum was fit with two Gaussian components at ~ 10 – 15 km s^{-1} and ~ 50 – 55 km s^{-1} . However, the residuals of this fit showed excess emission around 20–40 km s^{-1} , which we interpreted to be a third velocity component (see green dashed line in Figure 4). In our high-resolution data the 51.5 km s^{-1} component is the brightest emission in this region. The 10.6 km s^{-1} component is relatively faint compared to the other two components in the field. We have also analyzed the gas morphology in each component by isolating channels associated with each component (Figure 5). The morphology in all three components is unique.

2) Relationship between M0.10–0.08 and Orbital Stream 1: M0.10–0.08 is part of a larger structure of gas that contains the M–0.02–0.07 and M0.07–0.07 molecular clouds and has a velocity of around 50 km s^{-1} ([Tsuboi et al. 2011](#)). The central velocity of M0.10–0.08 (51.5 km s^{-1} ; Section 4.1) indicates that M0.10–0.08 is likely located on Orbital Stream 1 in the [Kruijssen et al. \(2015\)](#) model.

3) Resolving the Kinematics of M0.11–0.11: Discrepant reports regarding the central velocity of M0.11–0.11 range from 10 to 45 km s^{-1} . In our

high-resolution data, we detect two components in this velocity range: 10.6 and 37.6 km s^{-1} . We argue that gas in the 10.6 km s^{-1} component is associated with M0.11–0.11 as the morphology is distinct from that of the M0.10–0.08 cloud (Figure 5). Additionally, position-velocity analysis towards this region of the CMZ shows extended emission ($>70''$; >2.7 pc) from 0 to 20 km s^{-1} (Figure 7), that we suggest is associated with M0.11–0.11.

4) Physical Interaction Between M0.10–0.08 and M0.11–0.11: Past X-ray fluorescence observations by [Clavel et al. \(2013\)](#) show similar time delay signatures from both M0.10–0.08 and M0.11–0.11 and argue the two clouds are in the same physical position of the Galactic center. The intermediate morphology of the 37.6 km s^{-1} velocity component could be indicative of a physical interaction between M0.10–0.08 and M0.11–0.11. Indeed, all three velocity components appear to be connected in position-velocity space (Figure 7). The intermediate velocity component, which has similar features to both M0.10–0.08 and M0.11–0.11, could be gas from where these two are physically connected.

6. ACKNOWLEDGEMENTS

This material is based upon work supported by grants from the National Science Foundation (NSF; no. AST-0907934, AST-15243000, AST-1614782, AST-2008101, CAREER-2142300). Support for this work was also provided by the NSF through the Grote Reber Fellowship Program administered by Associated Universities, Inc./National Radio Astronomy Observatory.

NOB would like to thank Dr. Farhad Yusef-Zadah (Northwestern University), Dr. Robert Mutel (University of Iowa), Dr. Steven Spangler (University of Iowa), and Dr. Kenneth Gayley (University of Iowa) for their helpful critique on this thesis analysis. The authors would also like to thank Dr. Allison Costa (University of Virginia), Dr. Monica Sanchez (University of New Mexico), and Dr. Diederik Kruijssen (Max-Planck Institute) for their helpful insight on this work.

The authors would like to thank Dr. Elisabeth Mills (University of Kansas) for her helpful insight on the spectral line fitting and analysis of the results presented in this paper. The authors would also like to thank Dr. John Bally for his inspiration in creating the 3-color image shown in Figure 1. The authors would also like to thank the anonymous referee for their helpful insight on this manuscript.

Software: CASA ([International Consortium Of Scientists 2011](#)); *Clumpfind* ([Williams et al. 2011](#)); *pyspeckit* ([Ginsburg & Mirocha 2011](#); [Ginsburg et al. 2022](#))

APPENDIX

A. CATALOGUE OF CH₃OH MASERS IN M0.10–0.08

To catalogue the properties of these masers we used the *Clumpfind* algorithm (Williams et al. 1994). We define all compact sources with peak brightness temperatures above 400 K as CH₃OH masers in this paper, following the classification used in Mills et al. (2015). Table A.1 presents the properties of these 64 masers, with their spectra shown in Figure A.1. Table A.2 lists the maser candidates with their spectra shown in Figure A.2. Results of all 95 detected compact CH₃OH sources (both masers and candidate masers) are discussed in Section 3.3.

Table A.1. 36.2 GHz CH₃OH MASERS IN M0.10–0.08

ID	Maser Name	α	δ	v	FWHM	I_{peak}	Flux	T_b	Resolved?
		(J2000)	(J2000)	km s ⁻¹	km s ⁻¹	Jy b ⁻¹	Jy km s ⁻¹	K	
M1	M0.1039644-0.0802624	17 ^h 46 ^m 10 ^s .85	-28°53′21″.1	50.60	3.911	46.969	265.944	12438	YES
M2	M0.1072762-0.0845517	17 ^h 46 ^m 12 ^s .33	-28°53′18″.9	43.25	7.833	29.621	252.342	7844	YES
M3	M0.1033757-0.0817884	17 ^h 46 ^m 11 ^s .12	-28°53′25″.7	46.40	4.332	24.917	100.982	6598	NO
M4	M0.1100239-0.0810107	17 ^h 46 ^m 11 ^s .89	-28°53′03″.8	59.00	3.289	20.721	89.420	5487	YES
M5	M0.1038130-0.0832737	17 ^h 46 ^m 11 ^s .53	-28°53′27″.2	52.70	4.527	19.008	131.418	5033	YES
M6	M0.1096832-0.0812181	17 ^h 46 ^m 11 ^s .89	-28°53′05″.3	61.10	3.197	16.980	70.044	4496	YES
M7	M0.1090134-0.0860631	17 ^h 46 ^m 12 ^s .93	-28°53′16″.4	55.85	4.772	16.369	141.360	4334	YES
M8	M0.1035684-0.0824885	17 ^h 46 ^m 11 ^s .32	-28°53′26″.4	51.65	4.394	15.666	108.233	4148	YES
M9	M0.1078915-0.0897819	17 ^h 46 ^m 13 ^s .64	-28°53′26″.8	54.80	2.835	15.543	62.866	4116	NO
M10	M0.0997717-0.0798958	17 ^h 46 ^m 10 ^s .17	-28°53′33″.3	50.60	2.093	13.577	41.198	3595	NO
M11	M0.1068280-0.0840072	17 ^h 46 ^m 12 ^s .14	-28°53′19″.3	51.65	6.166	11.870	133.134	3143	YES
M12	M0.1072164-0.0806180	17 ^h 46 ^m 11 ^s .40	-28°53′11″.7	51.65	4.871	11.623	82.500	3078	YES
M13	M0.1026273-0.0797920	17 ^h 46 ^m 10 ^s .55	-28°53′24″.3	54.80	5.653	11.497	121.184	3044	YES
M14	M0.1081318-0.0846147	17 ^h 46 ^m 12 ^s .46	-28°53′16″.4	55.85	5.166	10.121	82.795	2680	YES
M15	M0.1078793-0.0799809	17 ^h 46 ^m 11 ^s .34	-28°53′08″.5	55.85	4.417	10.026	70.744	2655	YES
M16	M0.1117873-0.0839075	17 ^h 46 ^m 12 ^s .82	-28°53′03″.8	46.40	3.953	9.862	48.569	2611	NO
M17	M0.1032901-0.0791549	17 ^h 46 ^m 10 ^s .50	-28°53′21″.1	52.70	5.703	9.169	86.949	2428	YES
M18	M0.1054681-0.0800475	17 ^h 46 ^m 11 ^s .02	-28°53′16″.0	52.70	6.421	7.465	55.618	1977	YES
M19	M0.1048914-0.0886890	17 ^h 46 ^m 12 ^s .96	-28°53′34″.0	55.85	3.140	6.689	23.222	1771	NO
M20	M0.0961419-0.0793034	17 ^h 46 ^m 09 ^s .51	-28°53′43″.3	57.95	9.415	6.398	75.184	1694	YES
M21	M0.1090096-0.0854816	17 ^h 46 ^m 12 ^s .79	-28°53′15″.3	50.60	7.226	5.984	61.843	1584	YES
M22	M0.1089767-0.0909895	17 ^h 46 ^m 14 ^s .08	-28°53′25″.7	44.30	4.955	5.751	51.748	1522	YES
M23	M0.1090577-0.0849852	17 ^h 46 ^m 12 ^s .68	-28°53′14″.2	49.55	6.802	5.465	58.627	1447	YES
M24	M0.1115057-0.0826777	17 ^h 46 ^m 12 ^s .49	-28°53′02″.4	60.05	2.935	5.460	22.068	1445	NO
M25	M0.1066804-0.0902855	17 ^h 46 ^m 13 ^s .59	-28°53′31″.5	44.30	4.414	5.459	40.981	1445	YES
M26	M0.1034462-0.0820959	17 ^h 46 ^m 11 ^s .21	-28°53′26″.1	59.00	5.071	5.279	38.491	1398	YES
M27	M0.1084206-0.0843221	17 ^h 46 ^m 12 ^s .44	-28°53′15″.0	48.50	6.924	5.277	77.437	1397	YES
M28	M0.1051877-0.0895595	17 ^h 46 ^m 13 ^s .20	-28°53′34″.7	39.05	2.862	5.217	18.355	1381	YES
M29	M0.1101091-0.0809589	17 ^h 46 ^m 11 ^s .89	-28°53′03″.5	54.80	3.356	5.175	31.380	1370	YES
M30	M0.1062866-0.0796660	17 ^h 46 ^m 11 ^s .04	-28°53′12″.8	52.70	5.321	4.661	36.543	1234	YES
M31	M0.0958678-0.0792367	17 ^h 46 ^m 09 ^s .46	-28°53′44″.0	53.75	3.893	4.447	20.439	1177	NO
M32	M0.1096798-0.0833221	17 ^h 46 ^m 12 ^s .38	-28°53′09″.2	59.00	3.828	4.372	26.852	1157	NO
M33	M0.1107909-0.0832296	17 ^h 46 ^m 12 ^s .52	-28°53′05″.6	54.80	4.924	4.322	29.242	1144	NO
M34	M0.1095427-0.0832887	17 ^h 46 ^m 12 ^s .36	-28°53′09″.6	52.70	4.907	4.176	46.350	1105	YES
M35	M0.1064915-0.0901670	17 ^h 46 ^m 13 ^s .53	-28°53′31″.8	41.15	6.140	4.170	35.602	1104	YES
M36	M0.1022351-0.0825996	17 ^h 46 ^m 11 ^s .15	-28°53′30″.8	52.70	5.473	3.974	49.319	1052	YES
M37	M0.1065278-0.0825552	17 ^h 46 ^m 11 ^s .75	-28°53′17″.5	44.30	6.437	3.715	33.159	983	YES

M38	M0.1019943-0.0823959	17 ^h 46 ^m 11 ^s .07	-28°53'31''1	50.60	4.645	3.549	28.575	939	YES
M39	M0.1093989-0.0901487	17 ^h 46 ^m 13 ^s .94	-28°53'22''9	42.20	4.945	3.496	25.923	925	YES
M40	M0.1111797-0.0825258	17 ^h 46 ^m 12 ^s .41	-28°53'03''1	43.25	3.953	3.494	12.724	925	NO
M41	M0.1114205-0.0827295	17 ^h 46 ^m 12 ^s .49	-28°53'02''8	55.85	4.550	3.452	32.194	914	NO
M42	M0.1058716-0.0789844	17 ^h 46 ^m 10 ^s .82	-28°53'12''8	46.40	4.554	3.103	19.923	821	YES
M43	M0.1074210-0.0884336	17 ^h 46 ^m 13 ^s .26	-28°53'25''7	47.45	1.695	3.022	7.059	800	NO
M44	M0.1055756-0.0807994	17 ^h 46 ^m 11 ^s .21	-28°53'17''1	41.15	3.012	2.965	9.531	785	YES
M45	M0.1087352-0.0827294	17 ^h 46 ^m 12 ^s .11	-28°53'11''0	48.50	3.934	2.695	26.288	713	YES
M46	M0.1074951-0.0893226	17 ^h 46 ^m 13 ^s .48	-28°53'27''2	50.60	2.287	2.534	5.071	671	NO
M47	M0.1083131-0.0835702	17 ^h 46 ^m 12 ^s .25	-28°53'13''9	48.50	8.930	2.459	32.152	651	YES
M48	M0.1044687-0.0841590	17 ^h 46 ^m 11 ^s .84	-28°53'26''8	51.65	4.615	2.431	20.260	643	YES
M49	M0.1050284-0.0887224	17 ^h 46 ^m 12 ^s .98	-28°53'33''6	46.40	7.745	2.388	27.822	632	YES
M50	M0.1079693-0.0912524	17 ^h 46 ^m 14 ^s .00	-28°53'29''3	42.20	4.190	2.353	22.536	623	YES
M51	M0.1090804-0.0911599	17 ^h 46 ^m 14 ^s .13	-28°53'25''7	40.10	3.113	2.304	11.128	610	NO
M52	M0.0995238-0.0812144	17 ^h 46 ^m 10 ^s .44	-28°53'36''5	50.60	3.536	2.292	16.356	606	YES
M53	M0.1026091-0.0822551	17 ^h 46 ^m 11 ^s .12	-28°53'29''0	45.35	4.354	2.184	13.540	578	NO
M54	M0.1087914-0.0887671	17 ^h 46 ^m 13 ^s .53	-28°53'22''1	52.70	1.771	2.105	4.209	557	NO
M55	M0.1099096-0.0844667	17 ^h 46 ^m 12 ^s .68	-28°53'10''7	48.50	5.256	2.009	26.867	531	YES
M56	M0.1071396-0.0898893	17 ^h 46 ^m 13 ^s .56	-28°53'29''3	60.05	2.557	1.847	5.353	489	NO
M57	M0.1055655-0.0897965	17 ^h 46 ^m 13 ^s .31	-28°53'34''0	42.20	6.025	1.838	18.726	486	YES
M58	M0.1105910-0.0840519	17 ^h 46 ^m 12 ^s .68	-28°53'07''8	52.70	4.022	1.737	18.043	460	YES
M59	M0.1017160-0.0790623	17 ^h 46 ^m 10 ^s .25	-28°53'25''7	51.65	2.259	1.690	9.070	447	YES
M60	M0.1061836-0.0848665	17 ^h 46 ^m 12 ^s .25	-28°53'22''9	53.75	4.861	1.662	13.114	440	NO
M61	M0.1053243-0.0842220	17 ^h 46 ^m 11 ^s .97	-28°53'24''3	54.80	3.553	1.640	11.119	434	YES
M62	M0.1007572-0.0815144	17 ^h 46 ^m 10 ^s .69	-28°53'33''3	62.15	2.780	1.592	5.730	421	NO
M63	M0.1094015-0.0799883	17 ^h 46 ^m 11 ^s .56	-28°53'03''8	56.90	7.673	1.539	17.278	407	YES
M64	M0.0068760-0.0835109	17 ^h 46 ^m 12 ^s .03	-28°53'18''2	43.25	6.249	1.538	26.383	407	YES

Table A.2.36.2 GHz CH₃OH MASER CANDIDATES IN M0.10–0.08

ID	Maser Name	α (J2000)	δ (J2000)	v km s ⁻¹	FWHM km s ⁻¹	I_{peak} Jy b ⁻¹	Flux Jy km s ⁻¹	T_b K	Resolved?
CM1	M0.1017240-0.0829108	17 ^h 46 ^m 11 ^s .15	-28°53'32''9	55.85	6.634	1.498	20.043	396	YES
CM2	M0.1073500-0.0827553	17 ^h 46 ^m 11 ^s .92	-28°53'15''3	45.35	6.884	1.436	17.249	380	YES
CM3	M0.1087496-0.0796846	17 ^h 46 ^m 11 ^s .40	-28°53'05''3	63.20	6.767	1.418	17.226	375	YES
CM4	M0.1057278-0.0831589	17 ^h 46 ^m 11 ^s .78	-28°53'21''1	48.50	8.387	1.366	14.389	361	YES
CM5	M0.1114133-0.0842520	17 ^h 46 ^m 12 ^s .85	-28°53'05''6	50.60	3.705	1.365	8.593	361	YES
CM6	M0.0994242-0.0843109	17 ^h 46 ^m 11 ^s .15	-28°53'42''6	61.10	2.678	1.333	2.716	352	NO
CM7	M0.1073396-0.0890670	17 ^h 46 ^m 13 ^s .39	-28°53'27''2	44.30	1.908	1.323	2.607	350	NO
CM8	M0.1061099-0.0893484	17 ^h 46 ^m 13 ^s .28	-28°53'31''5	52.70	2.900	1.252	5.884	331	YES
CM9	M0.1073796-0.0820367	17 ^h 46 ^m 11 ^s .75	-28°53'13''9	41.15	6.005	1.210	10.429	320	NO
CM10	M0.1069128-0.0812699	17 ^h 46 ^m 11 ^s .51	-28°53'13''9	46.40	6.136	1.199	9.117	317	YES
CM11	M0.1054022-0.0856925	17 ^h 46 ^m 12 ^s .33	-28°53'26''8	53.75	1.864	1.165	3.439	308	NO
CM12	M0.1037539-0.0847109	17 ^h 46 ^m 11 ^s .86	-28°53'30''0	53.75	2.552	1.063	6.657	281	YES
CM13	M0.1025205-0.0844109	17 ^h 46 ^m 11 ^s .62	-28°53'33''3	53.75	1.525	1.020	1.581	270	NO
CM14	M0.1086098-0.0871261	17 ^h 46 ^m 13 ^s .12	-28°53'19''6	59.00	8.039	0.989	8.824	261	YES
CM15	M0.1034571-0.0811550	17 ^h 46 ^m 10 ^s .99	-28°53'24''3	56.90	5.577	0.987	9.074	261	YES
CM16	M0.0998050-0.0797587	17 ^h 46 ^m 10 ^s .14	-28°53'32''9	56.90	3.739	0.945	5.708	250	NO
CM17	M0.1070237-0.0799179	17 ^h 46 ^m 11 ^s .21	-28°53'11''0	60.05	7.663	0.930	11.283	246	YES

CM18	M0.1080322-0.0903968	17 ^h 46 ^m 13 ^s .80	-28°53'27".5	41.15	4.784	0.889	7.060	235	YES
CM19	M0.1053015-0.0807328	17 ^h 46 ^m 11 ^s .15	-28°53'17".8	45.35	4.598	0.860	7.262	227	YES
CM20	M0.0989385-0.0806366	17 ^h 46 ^m 10 ^s .22	-28°53'37".2	53.75	5.362	0.855	6.528	226	YES
CM21	M0.1002794-0.0816885	17 ^h 46 ^m 10 ^s .66	-28°53'35".1	49.55	2.898	0.824	6.111	218	YES
CM22	M0.1051058-0.0848221	17 ^h 46 ^m 12 ^s .08	-28°53'26".1	52.70	3.773	0.819	5.464	216	YES
CM23	M0.1093610-0.0816478	17 ^h 46 ^m 11 ^s .94	-28°53'07".1	55.85	4.041	0.811	4.470	214	YES
CM24	M0.1043426-0.0831849	17 ^h 46 ^m 11 ^s .59	-28°53'25".4	45.35	8.092	0.730	5.279	193	YES
CM25	M0.1015946-0.0840405	17 ^h 46 ^m 11 ^s .40	-28°53'35".4	48.50	2.788	0.678	2.904	179	YES
CM26	M0.1090351-0.0814959	17 ^h 46 ^m 11 ^s .86	-28°53'07".8	52.70	4.308	0.668	2.702	176	NO
CM27	M0.1083018-0.0818256	17 ^h 46 ^m 11 ^s .84	-28°53'10".6	45.35	4.275	0.586	4.017	155	NO
CM28	M0.1074053-0.0807365	17 ^h 46 ^m 11 ^s .45	-28°53'11".4	47.45	4.038	0.572	3.719	151	YES
CM29	M0.1016794-0.0813032	17 ^h 46 ^m 10 ^s .77	-28°53'30".0	48.50	<1.05	0.540	0.553	143	NO
CM30	M0.1987015-0.0810144	17 ^h 46 ^m 10 ^s .28	-28°53'38".7	43.25	<1.05	0.504	0.365	133	NO
CM31	M0.1044869-0.0816958	17 ^h 46 ^m 11 ^s .26	-28°53'22".1	62.15	4.628	0.421	4.661	111	YES

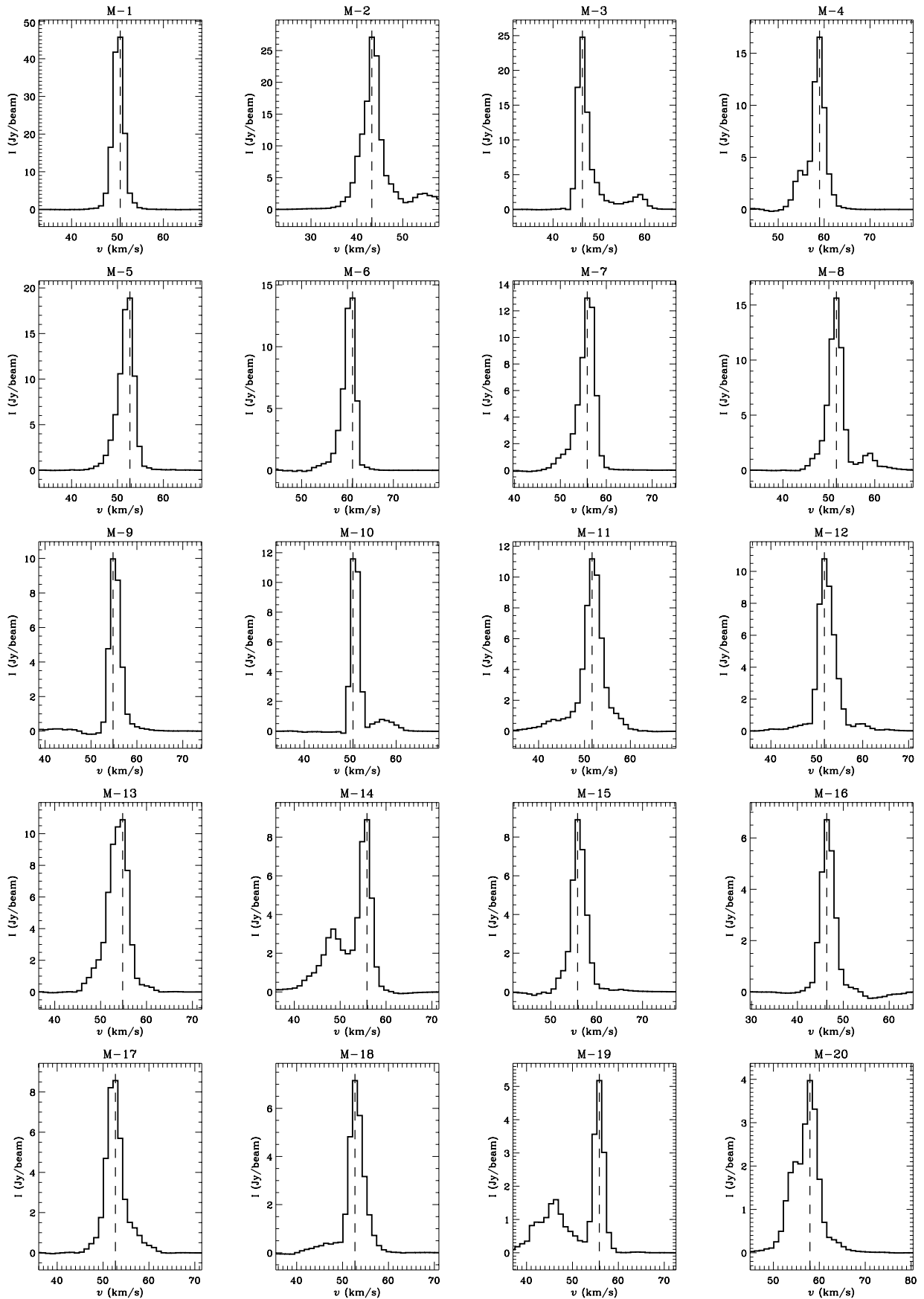


Figure A.1. Spectra of detected 36 GHz CH_3OH masers in M0.10-0.08.

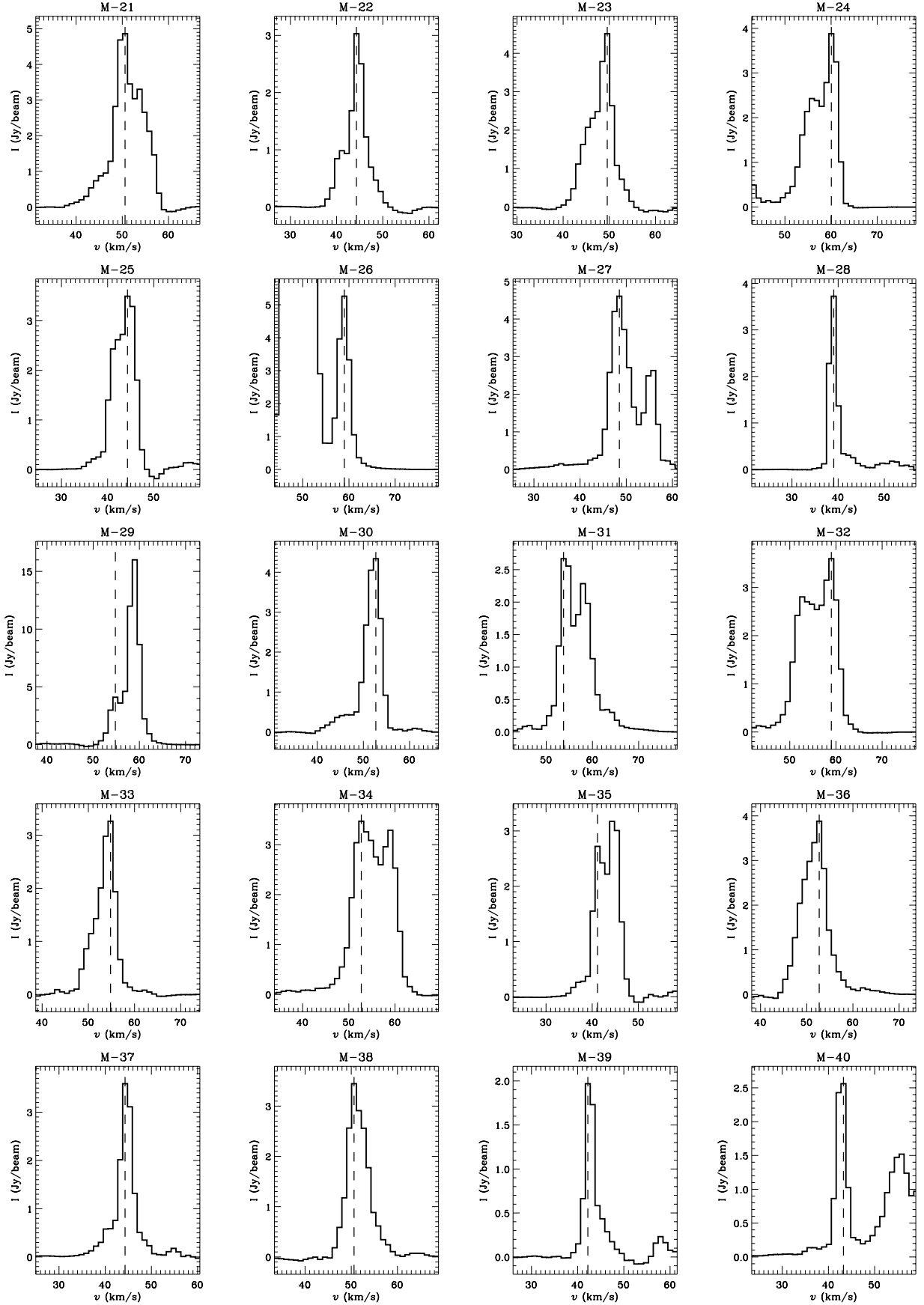


Figure A.1. (Continued)

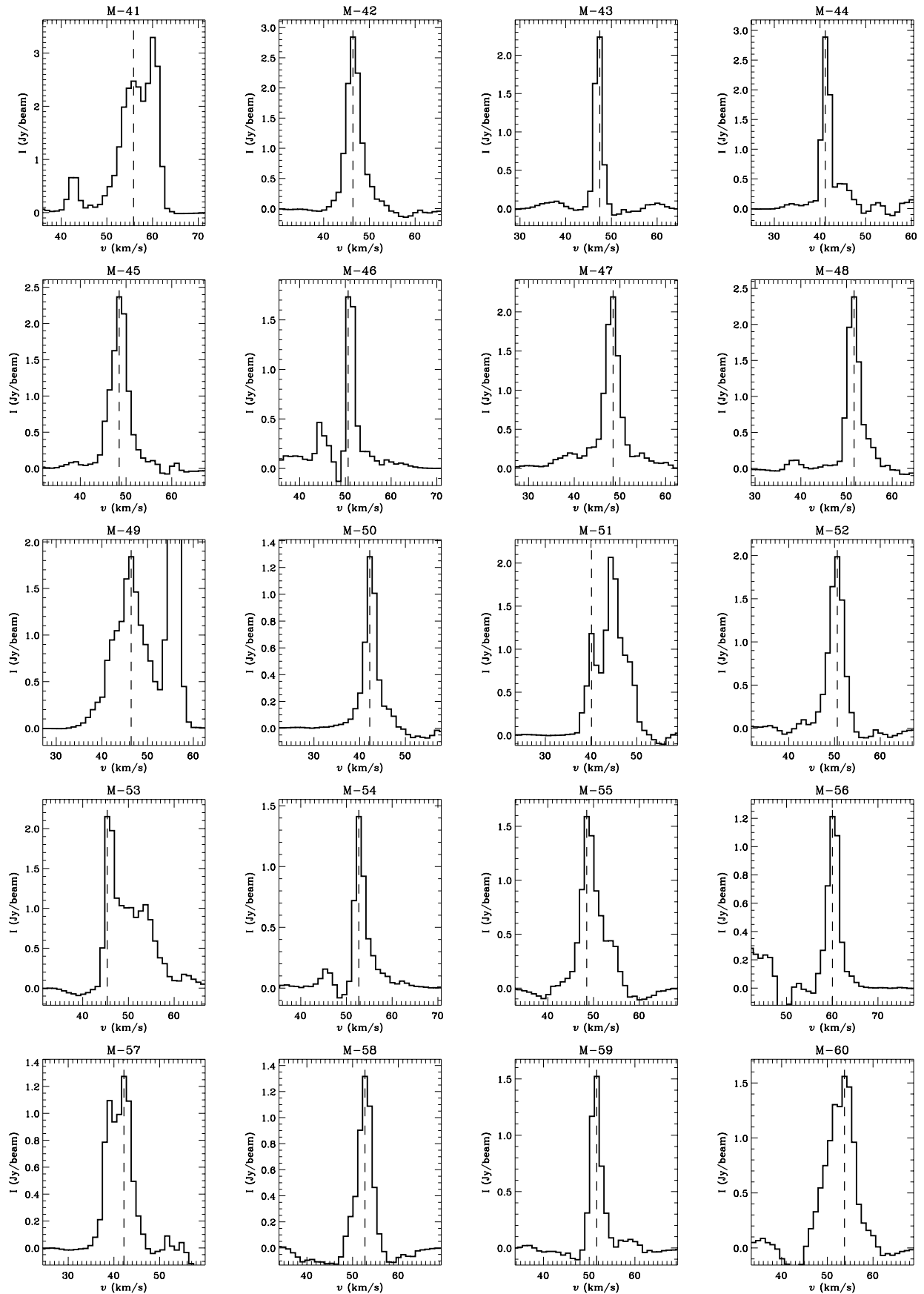


Figure A.1. (Continued)

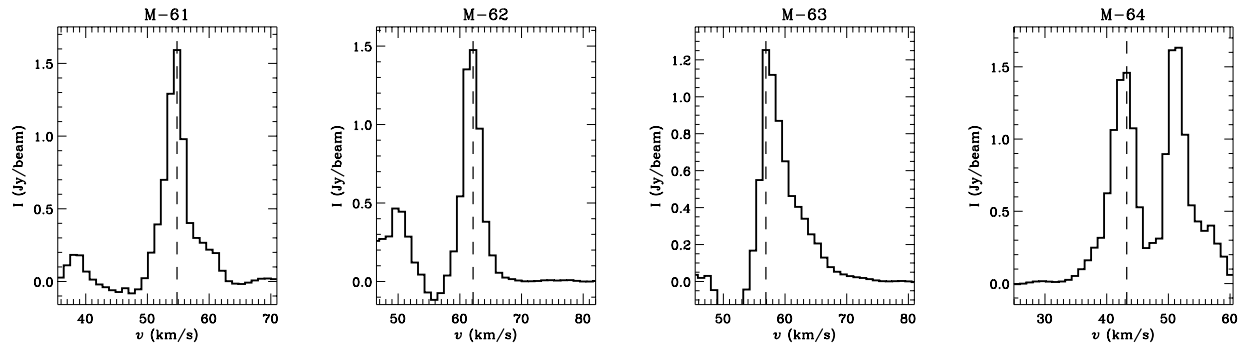


Figure A.1. (Continued)

REFERENCES

- Bally, J., Stark, A. A., Wilson, R. W., & Henkel, C. 1987, *ApJS*, 65, 13, doi: [10.1086/191217](https://doi.org/10.1086/191217)
- Battersby, C., Keto, E., Walker, D., et al. 2020, *ApJS*, 249, 35, doi: [10.3847/1538-4365/aba18e](https://doi.org/10.3847/1538-4365/aba18e)
- Butterfield, N., Lang, C. C., Morris, M., Mills, E. A. C., & Ott, J. 2018, *ApJ*, 852, 11, doi: [10.3847/1538-4357/aa886e](https://doi.org/10.3847/1538-4357/aa886e)
- Churchwell, E., Babler, B. L., Meade, M. R., et al. 2009, *PASP*, 121, 213, doi: [10.1086/597811](https://doi.org/10.1086/597811)
- Chuss, D. T., Davidson, J. A., Dotson, J. L., et al. 2003, *ApJ*, 599, 1116, doi: [10.1086/379538](https://doi.org/10.1086/379538)
- Clavel, M., Terrier, R., Goldwurm, A., et al. 2013, *A&A*, 558, A32, doi: [10.1051/0004-6361/201321667](https://doi.org/10.1051/0004-6361/201321667)
- Cotton, W. D., & Yusef-Zadeh, F. 2016, *ApJS*, 227, 10, doi: [10.3847/0067-0049/227/1/10](https://doi.org/10.3847/0067-0049/227/1/10)
- Cramphorn, C. K., & Sunyaev, R. A. 2002, *A&A*, 389, 252, doi: [10.1051/0004-6361:20020521](https://doi.org/10.1051/0004-6361:20020521)
- Do, T., Hees, A., Ghez, A., et al. 2019, *Science*, 365, 664, doi: [10.1126/science.aav8137](https://doi.org/10.1126/science.aav8137)
- Fukui, Y., Iguchi, T., Kaifu, N., et al. 1977, *PASJ*, 29, 643
- Fukui, Y., Torii, K., Ohama, A., et al. 2016, *ApJ*, 820, 26, doi: [10.3847/0004-637X/820/1/26](https://doi.org/10.3847/0004-637X/820/1/26)
- Ginsburg, A., & Mirocha, J. 2011, PySpecKit: Python Spectroscopic Toolkit, Astrophysics Source Code Library. <http://ascl.net/1109.001>
- Ginsburg, A., Sokolov, V., de Val-Borro, M., et al. 2022, *AJ*, 163, 291, doi: [10.3847/1538-3881/ac695a](https://doi.org/10.3847/1538-3881/ac695a)
- Ginsburg, A., Henkel, C., Ao, Y., et al. 2016, *A&A*, 586, A50, doi: [10.1051/0004-6361/201526100](https://doi.org/10.1051/0004-6361/201526100)
- Guan, Y., Clark, S. E., Hensley, B. S., et al. 2021, *ApJ*, 920, 6, doi: [10.3847/1538-4357/ac133f](https://doi.org/10.3847/1538-4357/ac133f)
- Güsten, R., Walmsley, C. M., & Pauls, T. 1981, *A&A*, 103, 197
- Handa, T., Sakano, M., Naito, S., Hiramatsu, M., & Tsuboi, M. 2006, *ApJ*, 636, 261, doi: [10.1086/497881](https://doi.org/10.1086/497881)
- Hatchfield, H. P., Battersby, C., Keto, E., et al. 2020, *ApJS*, 251, 14, doi: [10.3847/1538-4365/abb610](https://doi.org/10.3847/1538-4365/abb610)
- Haworth, T. J., Tasker, E. J., Fukui, Y., et al. 2015, *MNRAS*, 450, 10, doi: [10.1093/mnras/stv639](https://doi.org/10.1093/mnras/stv639)
- Henshaw, J. D., Longmore, S. N., Kruijssen, J. M. D., et al. 2016, *MNRAS*, 457, 2675, doi: [10.1093/mnras/stw121](https://doi.org/10.1093/mnras/stw121)
- International Consortium Of Scientists. 2011, CASA: Common Astronomy Software Applications, Astrophysics Source Code Library. <http://ascl.net/1107.013>
- Jones, P. A., Burton, M. G., Cunningham, M. R., et al. 2012, *MNRAS*, 419, 2961, doi: [10.1111/j.1365-2966.2011.19941.x](https://doi.org/10.1111/j.1365-2966.2011.19941.x)
- Kauffmann, J., Pillai, T., Zhang, Q., et al. 2017, *A&A*, 603, A89, doi: [10.1051/0004-6361/201628088](https://doi.org/10.1051/0004-6361/201628088)
- Krieger, N., Ott, J., Beuther, H., et al. 2017, *ApJ*, 850, 77, doi: [10.3847/1538-4357/aa951c](https://doi.org/10.3847/1538-4357/aa951c)
- Kruijssen, J. M. D., Dale, J. E., & Longmore, S. N. 2015, *MNRAS*, 447, 1059, doi: [10.1093/mnras/stu2526](https://doi.org/10.1093/mnras/stu2526)
- Ludovici, D. A., Lang, C. C., Morris, M. R., et al. 2016, *ApJ*, 826, 218, doi: [10.3847/0004-637X/826/2/218](https://doi.org/10.3847/0004-637X/826/2/218)
- Mauersberger, R., Henkel, C., Wilson, T. L., & Walmsley, C. M. 1986, *A&A*, 162, 199
- McMullin, J. P., Waters, B., Schiebel, D., Young, W., & Golap, K. 2007, in *Astronomical Society of the Pacific Conference Series*, Vol. 376, *Astronomical Data Analysis Software and Systems XVI*, ed. R. A. Shaw, F. Hill, & D. J. Bell, 127
- Menten, K. 1991, in *Astronomical Society of the Pacific Conference Series*, Vol. 16, *Atoms, Ions and Molecules: New Results in Spectral Line Astrophysics*, ed. A. D. Haschick & P. T. P. Ho, 119
- Mills, E. A. C., & Battersby, C. 2017, *ApJ*, 835, 76, doi: [10.3847/1538-4357/835/1/76](https://doi.org/10.3847/1538-4357/835/1/76)
- Mills, E. A. C., Butterfield, N., Ludovici, D. A., et al. 2015, *ApJ*, 805, 72, doi: [10.1088/0004-637X/805/1/72](https://doi.org/10.1088/0004-637X/805/1/72)

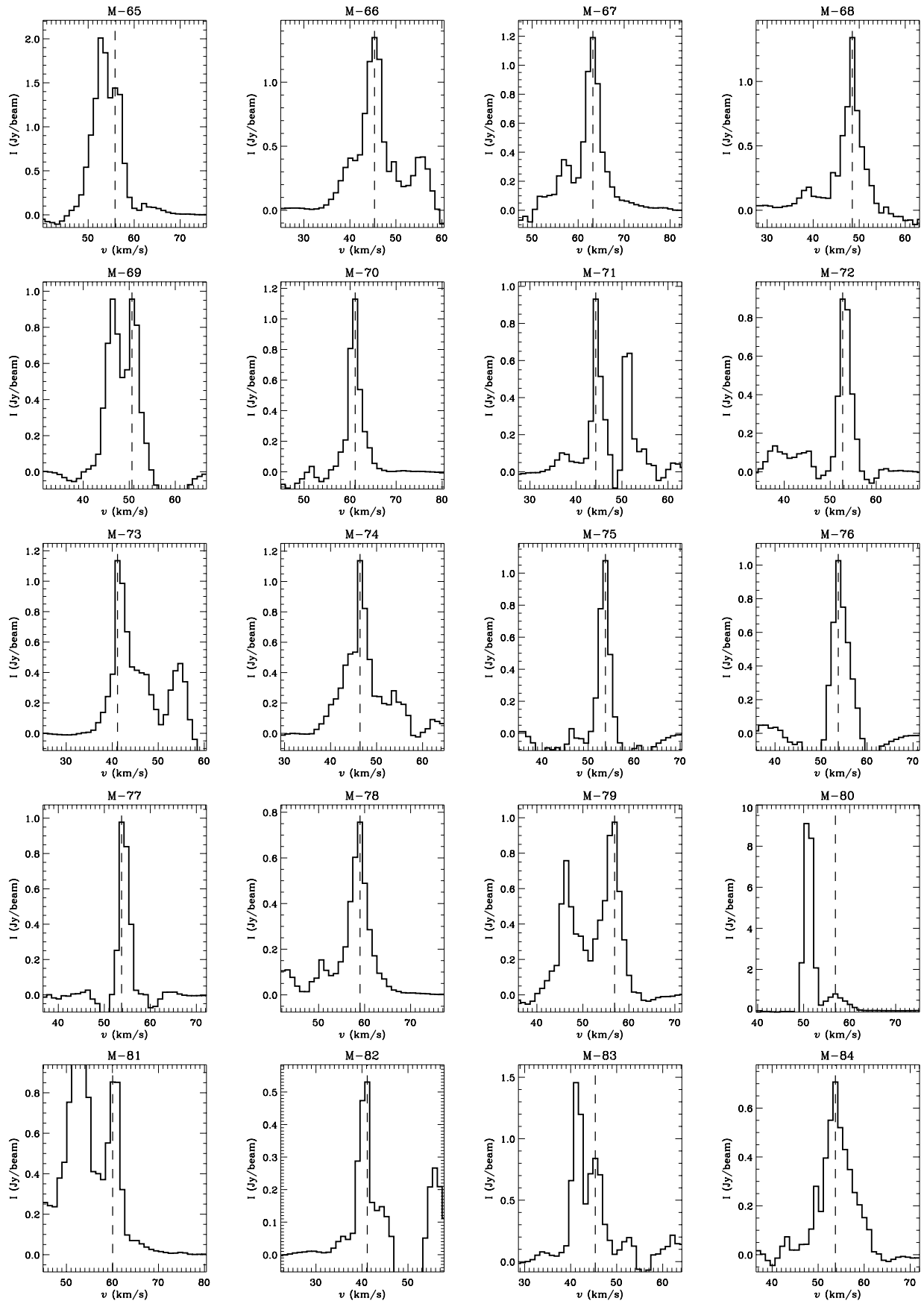


Figure A.2. maser candidates CM1(M65) to CM16(M60)

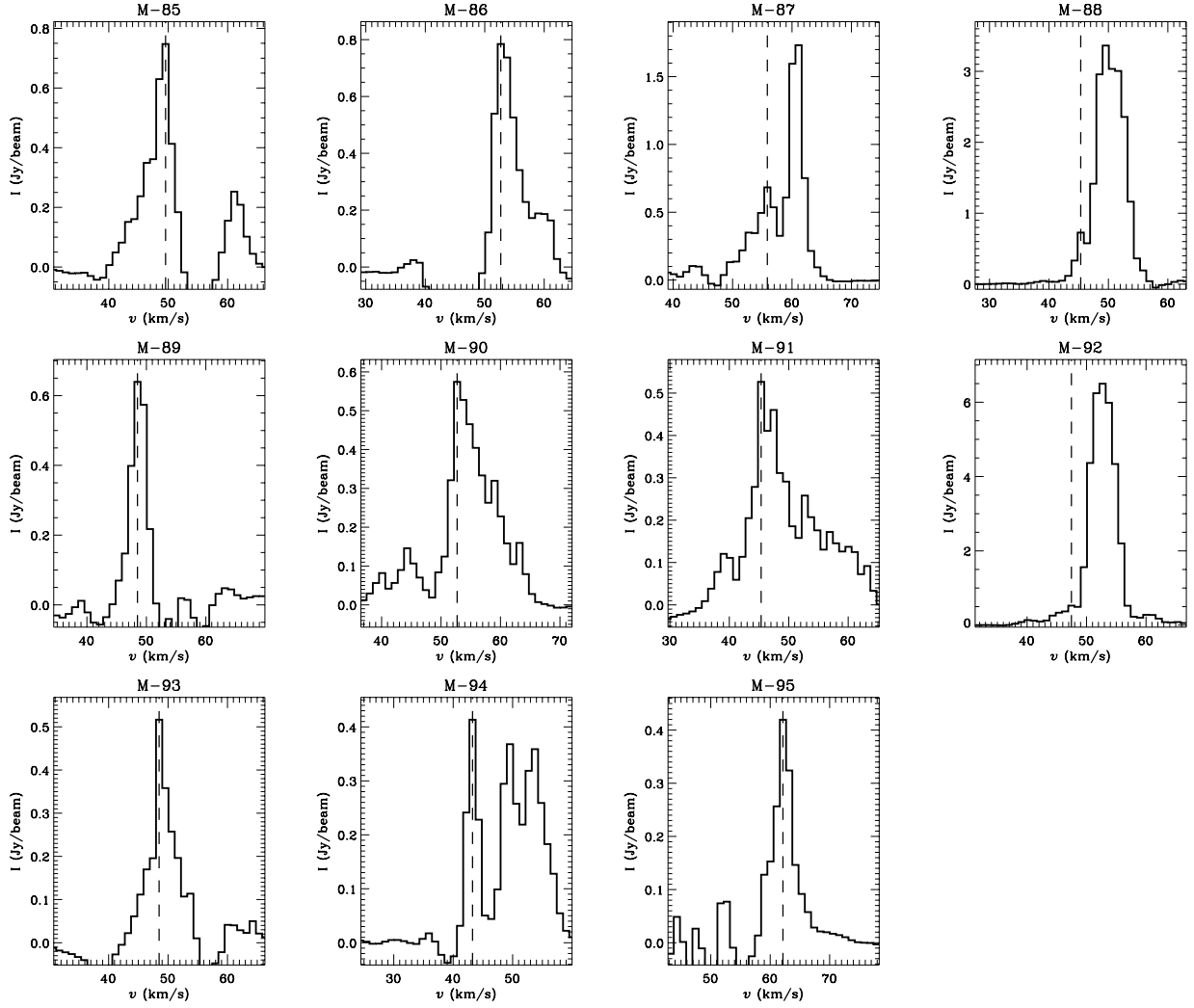


Figure A.2. (Continued)

- Mills, E. A. C., Ginsburg, A., Immer, K., et al. 2018a, *ApJ*, 868, 7, doi: [10.3847/1538-4357/aae581](https://doi.org/10.3847/1538-4357/aae581)
- Mills, E. A. C., Lang, C. C., Morris, M. R., et al. 2014, in *IAU Symposium*, Vol. 303, *The Galactic Center: Feeding and Feedback in a Normal Galactic Nucleus*, ed. L. O. Sjouwerman, C. C. Lang, & J. Ott, 139–143, doi: [10.1017/S1743921314000398](https://doi.org/10.1017/S1743921314000398)
- Mills, E. A. C., & Morris, M. R. 2013, *ApJ*, 772, 105, doi: [10.1088/0004-637X/772/2/105](https://doi.org/10.1088/0004-637X/772/2/105)
- Mills, E. A. C., Ginsburg, A., Clements, A. R., et al. 2018b, *ApJL*, 869, L14, doi: [10.3847/2041-8213/aaf237](https://doi.org/10.3847/2041-8213/aaf237)
- Molinari, S., Swinyard, B., Bally, J., et al. 2010, *PASP*, 122, 314, doi: [10.1086/651314](https://doi.org/10.1086/651314)
- Molinari, S., Bally, J., Noriega-Crespo, A., et al. 2011, *ApJL*, 735, L33, doi: [10.1088/2041-8205/735/2/L33](https://doi.org/10.1088/2041-8205/735/2/L33)
- Morimoto, M., Kanzawa, T., & Ohishi, M. 1985, *ApJL*, 288, L11, doi: [10.1086/184411](https://doi.org/10.1086/184411)
- Ponti, G., Terrier, R., Goldwurm, A., Belanger, G., & Trap, G. 2010, *ApJ*, 714, 732, doi: [10.1088/0004-637X/714/1/732](https://doi.org/10.1088/0004-637X/714/1/732)
- Sawada, T., Hasegawa, T., Handa, T., & Cohen, R. J. 2004, *MNRAS*, 349, 1167, doi: [10.1111/j.1365-2966.2004.07603.x](https://doi.org/10.1111/j.1365-2966.2004.07603.x)
- Sjouwerman, L. O., Pihlström, Y. M., & Fish, V. L. 2010, *ApJL*, 710, L111, doi: [10.1088/2041-8205/710/2/L111](https://doi.org/10.1088/2041-8205/710/2/L111)
- Sofue, Y. 1995, *PASJ*, 47, 527, <https://arxiv.org/abs/astro-ph/9508110>
- Sunyaev, R., & Churazov, E. 1998, *MNRAS*, 297, 1279, doi: [10.1046/j.1365-8711.1998.01684.x](https://doi.org/10.1046/j.1365-8711.1998.01684.x)
- Takahira, K., Tasker, E. J., & Habe, A. 2014, *ApJ*, 792, 63, doi: [10.1088/0004-637X/792/1/63](https://doi.org/10.1088/0004-637X/792/1/63)
- Terrier, R., Clavel, M., Soldi, S., et al. 2018, *A&A*, 612, A102, doi: [10.1051/0004-6361/201730837](https://doi.org/10.1051/0004-6361/201730837)
- Torii, K., Hattori, Y., Hasegawa, K., et al. 2017, *ApJ*, 835, 142, doi: [10.3847/1538-4357/835/2/142](https://doi.org/10.3847/1538-4357/835/2/142)
- Tsuboi, M., Tadaki, K.-I., Miyazaki, A., & Handa, T. 2011, *PASJ*, 63, 763, doi: [10.1093/pasj/63.4.763](https://doi.org/10.1093/pasj/63.4.763)
- Tsuboi, M., Ukita, N., & Handa, T. 1997, *ApJ*, 481, 263
- Williams, J. P., de Geus, E. J., & Blitz, L. 1994, *ApJ*, 428, 693, doi: [10.1086/174279](https://doi.org/10.1086/174279)
- . 2011, *Clumpfind: Determining Structure in Molecular Clouds*, *Astrophysics Source Code Library*, doi: [10.1086/174279](https://doi.org/10.1086/174279)
- Yusef-Zadeh, F., Cotton, W., Viti, S., Wardle, M., & Royster, M. 2013, *ApJL*, 764, L19, doi: [10.1088/2041-8205/764/2/L19](https://doi.org/10.1088/2041-8205/764/2/L19)
- Zylka, R., Guesten, R., Henkel, C., & Batrla, W. 1992, *A&AS*, 96, 525